

Reconstruction of Dark Matter and Baryon Density From Galaxies: A Comparison of Linear, Halo Model and Machine Learning-Based Methods

Jordan Krywonos^{b,c} Yurii Kvasiuk^a Matthew C. Johnson^{b,c}
Moritz Münchmeyer^{a,d}

^aDepartment of Physics, University of Wisconsin-Madison, Madison, WI 53706, USA

^bPerimeter Institute for Theoretical Physics, Waterloo, ON N2L 2Y5, Canada

^cDepartment of Physics and Astronomy, York University, Toronto, ON M3J 1P3, Canada

^dNSF-Simons AI Institute for the Sky (SkAI), 172 E. Chestnut St., Chicago, IL 60611, USA

E-mail: jkrywonos@perimeterinstitute.ca, kvasiuk@wisc.edu,
mjohnson@perimeterinstitute.ca, muenchmeyer@wisc.edu

Abstract. For many analyses in cosmology it is necessary to reconstruct the likely distribution of unobserved fields, such as dark matter or baryons, from observed luminous tracers. The dominant approach in cosmology has been to use the so-called halo model, which assumes radially symmetric profiles centered around luminous tracers such as galaxies. More recently, field-level machine learning methods have been proposed that can learn to estimate the unobserved field after being trained on simulations. However, it is unclear whether machine learning methods indeed significantly improve over linear methods or the halo model. In this paper we make a systematic comparison of different approaches to reconstruct dark matter and baryons from galaxy data using the CAMELS simulations. We find the best results using a combined GNN-CNN approach. We also provide a general analysis and visualization of the relationship of matter, baryons, halos and galaxies in these simulations to interpret our results.

Contents

1	Introduction	1
2	Overview of Approaches to Reconstruct Unobserved Fields	3
3	Simulation Data	6
3.1	Dataset	6
3.2	Visualizing the Data	7
4	Methods	8
4.1	Performance Metric	8
4.2	Baseline: Simple Grid Assignment and Linear Transfer Function	9
4.3	NFW Painting of Individual Halo Profiles	11
4.4	Halo-Level Machine Learning: GNN-NFW Painting	12
4.4.1	Architecture	12
4.4.2	Training	12
4.4.3	GNN-NFW Profile Painting	13
4.5	Field-Level Machine Learning: GNN-CNN Approach	13
4.5.1	Architecture	13
4.5.2	Training	13
5	Results: Dark Matter Reconstruction	14
5.1	Summary of Results	14
5.2	Baseline: Linear Transfer Function	14
5.3	NFW Painting of Individual Halo Profiles	14
5.4	Halo-Level Machine Learning: GNN-NFW	17
5.5	Field-Level Machine Learning: GNN-CNN	19
6	Results: Gas Reconstruction	20
7	Robustness Against Unknown Feedback Parameters	22
8	Outlook: Using the Model for Parameter Inference	23
9	Conclusions and Outlook	25
	References	27

1 Introduction

Within the Λ CDM paradigm, dark matter provides the scaffolding on which structure forms, and baryonic matter, which we will refer to as ‘gas’, provides the medium from which astrophysical objects like stars and galaxies form and evolve. Dark matter, and the majority of gas, is not directly observable. Instead, we observe luminous tracers, e.g. starlight from galaxies or thermal radiation from hot gas, that are embedded within the underlying non-luminous dark matter and gas. It is possible to observe the interaction of photons with dark matter

and gas, e.g. through weak gravitational lensing or the kinetic Sunyaev Zel’dovich effect, but this will not be the focus here. Instead, we are concerned with how luminous tracers can be used to make field-level inferences about the distribution of dark matter and gas. Working at the field-level, as opposed to focusing on summary statistics like power spectra, has the advantage of preserving the maximum amount of cosmological information (see e.g. Ref. [1]). Some applications of field-level inference include: incorporating non-Gaussian information in cosmological parameter constraints, incorporating the effect of survey geometry and systematics, testing the environmental-dependence of galaxy formation, and creating templates for cross-correlation studies.

Making field-level inferences requires a model for the connection between luminous tracers and the underlying dark matter and gas. A dominant paradigm for understanding this connection is the halo model of large-scale structure (see e.g. Refs. [2, 3]). Within this construction, all dark matter is assumed to be bound into halos whose positions are correlated by the long-wavelength density field. Each halo is populated with gas or galaxies according to a set of theoretical prescriptions, with parameters calibrated by matching a variety of observations. For galaxies this is referred to as the ‘Galaxy-Halo Connection’ (see e.g. Ref. [4] for a review) and the (probabilistic) set of rules for populating halos with galaxies is the Halo Occupation Distribution (HOD). The HOD depends on the properties of the galaxy sample and dark matter mass of the halo, but might also depend on more complex physics, e.g. the assembly history (a recent assessment can be found here [5]). For gas, a simple model could be a parameterized spherically-symmetric density profile that depends on halo mass (a recent example can be found in Ref. [6]). This profile may be derived based on physical principles, e.g. hydrostatic equilibrium, or measured from hydrodynamic simulations or observations. For computing summary statistics, the halo model provides a physically-motivated description that can be fit to data in order to make inferences about cosmology, galaxies, and gas. However, there are limitations to this approach such as the non-conservation of mass and a poor description of intermediate scales (the halo model can be modified to mitigate these shortcomings, e.g. [7, 8]).

It is also possible to apply the halo model at the field-level. The simplest example of this would be to create a linear transfer function in Fourier space that relates a tracer to the underlying dark matter distribution (see e.g. Ref. [9] for a recent example). The filter leading to the minimum variance estimate of the dark matter field is the cross-power spectrum between the tracer and dark matter, normalized by the auto-spectrum of the tracer, both computed using the halo model (for an example see e.g. Ref. [10]). On linear scales, this corresponds to dividing the tracer field by its linear bias with respect to dark matter. On smaller scales, non-linear effects – such as baryonic feedback and non-linear gravitational evolution – become significant, causing the linear transfer function approach to break down. Another technique that can be applied at the field level is halo abundance matching (HAM) [11–13]. This technique relates a halo quantity (eg. halo mass M_h) to a galaxy quantity (eg. stellar mass M_*) by assuming a monotonic relation and matching the cumulative abundances ($n_h(> M_h) = n_g(> M_*)$). One can then assign dark matter masses to the position of each galaxy to create an estimate of the density field. A downside is that HAM is limited to using only a single galaxy property to infer the host halo characteristics. The HAM approach can be generalized to include more information about the distribution of density in dark matter halos. For example, instead of assigning a mass to the position of the halo, one could ‘paint’ on the associated dark matter density profile, e.g. the Navarro-Frank-White (NFW) profile.

The linear transfer function and HAM approaches described above rely on linear corre-

lations (between fields and galaxy - halo properties, respectively). Non-linear methods can in principle capture more cosmological information, improving our inference of the distribution of dark matter from luminous tracers. One approach that has been extensively explored in the literature is to forward-model galaxy surveys, sampling Gaussian initial conditions, evolving them with N-body simulations, creating mock galaxy surveys and comparing the mocks with data to find the most likely underlying dark matter distribution [14–17]. This approach is based on causal inferences (because samples are generated by evolving initial conditions with physical equations of motion) rather than linear correlation, and the statistical distribution over initial conditions is Gaussian, allowing precisely defined error bars. However, sampling a large range of scales is computationally challenging. We do not pursue this class of methods further in this work. Another set of approaches relies on machine learning (ML) methods. ML offers a powerful framework for handling high-dimensional problems and capturing complex relationships across a range of scales. For example, Refs. [18–23] use ML to improve on HAM by predicting halo masses from a variety of galaxy properties in addition to stellar mass. At the field level, Refs. [24, 25] employ diffusion models to reconstruct 2D dark matter fields from galaxy distributions. These approaches can be far more computationally efficient than full forward-modeling, but rely on correlation (no explicit causal inference), and error bars are not rigorously defined from Gaussian initial conditions.

At a basic level, the problem we wish to solve is to find the statistically ideal non-linear map between a point cloud (galaxies) and a pixelated continuous field (dark matter or gas). A class of ML architectures well-suited to point clouds are graph neural networks (GNN); see e.g. [26]. The GNN architecture encodes galaxy features in nodes, and relational information (e.g. relative distance) in vertices connecting them. GNNs have successfully been used to infer the mass of individual halos from galaxy features e.g. [27, 28] or cosmological parameters e.g. [29]. A class of ML architectures well-suited to pixelated continuous fields, a type of regular grid-structured data, are convolutional neural networks (CNN). CNNs have been applied to a wide variety of problems in cosmology e.g. Refs. [30–40]. In Ref. [41], we introduced a hybrid architecture in which a GNN step is used to map galaxies to dark matter halos and a CNN step is used to map the halo distribution to an inference of the dark matter field in three dimensions. Training the network on the CAMELS suite of cosmological simulations [42–45], we demonstrated that such a GNN-CNN hybrid architecture could outperform the linear transfer function or a gridded halo mass assignment.

In this paper, we undertake a detailed study of the capabilities of a GNN-CNN hybrid architecture to reconstruct the dark matter field from galaxies, comparing the fidelity of the reconstruction to a variety of other techniques based on the halo model. We provide a detailed visualization of the reconstructed dark matter field using different techniques, highlighting the features that are captured and those that are not. We demonstrate that the GNN-CNN reconstruction trained on CAMELS is superior to halo-model based approaches, and investigate its robustness with respect to unknown feedback parameters. Finally, we comment on cosmological and astrophysical parameter inference using this reconstruction.

2 Overview of Approaches to Reconstruct Unobserved Fields

The goal of this paper is to reconstruct the unobserved matter distribution δ_m and the unobserved baryon distribution δ_e from the observed galaxy density δ_g . In this section, we first give a high-level overview of several possible reconstruction methods.

Linear transfer function. A common approach is to use a linear transfer function in Fourier space to approximate the target field from the observed field:

$$\hat{\delta}_m(\mathbf{k}) = T(k) \delta_g^{\text{obs}}(\mathbf{k}) \quad (2.1)$$

The choice of linear transfer function that minimizes $\langle |\hat{\delta}_m(\mathbf{k}) - \delta_m(\mathbf{k})|^2 \rangle$ is the ratio of cross- to auto-power spectra

$$T(k) = \frac{P_{gm}(k)}{P_{gg}(k)}. \quad (2.2)$$

The transfer function in Eq. (2.2) can be derived by assuming that g and m are correlated Gaussian random fields and that g is observed with some shot noise (included in P_{gg}). A different possibility would be to use the transfer function of form

$$T(k) = \frac{\sqrt{P_{mm}(k)}}{\sqrt{P_{gg}(k)}}. \quad (2.3)$$

as studied for example in [46] in the context of mapping N-body to hydrodynamic simulations, which would make the power spectrum correct by definition.

Of course, a linear transfer function can never improve the cross-correlation coefficient between the observed field and the target field. We also note that a linear transfer function can always be added to other methods, to enforce that the reconstructed field has any desired power spectrum. Note however, that one does not always want the power spectrum of the reconstructed field to be equal to the target field. Often, the output should be inverse covariance weighted so that noisy (small-scale) modes are suppressed. In the above transfer function Eq. (2.2), this will happen if P_{gg} includes the galaxy shot noise.

Halo painting. A method to make a template for dark matter or baryons from galaxies is to identify the dark matter halo that corresponds to a group of galaxies, and then assign a NFW profile (for dark matter) or a gas profile (for baryons) centered on that halo. This mirrors how the cross-correlation of galaxies and dark matter or baryons is calculated in the halo model. This type of ‘painting’ on the location of halos is commonly employed in creating mock observables from dark matter-only simulations, see e.g. [47–50]. In pixel space, we can think of the linear transfer function defined in Eq. (2.2) as a simple example of this, where an identical density profile is painted on the position of each galaxy. This can be seen by writing the galaxy field as a sum over delta functions

$$\delta_g^{\text{obs}}(\vec{x}) = \sum_{i=1}^{N_g} \delta^{(3)}(\vec{x} - \vec{x}_i) \quad (2.4)$$

and noting that the Fourier transform of the transfer function is spherically symmetric and given by

$$T(|\vec{x}|) \equiv \int \frac{d^3k}{(2\pi)^3} \frac{P_{gm}(k)}{P_{gg}(k)} e^{i\vec{k} \cdot \vec{x}} \quad (2.5)$$

The dark matter density field is then

$$\delta_m(\vec{x}) = \int d^3y T(|\vec{x} - \vec{y}|) \sum_{i=1}^{N_g} \delta^{(3)}(\vec{y} - \vec{x}_i) \quad (2.6)$$

$$= \sum_{i=1}^{N_g} T(|\vec{x} - \vec{x}_i|) \quad (2.7)$$

The profile painted on top of each galaxy position is the inverse Fourier transform of the transfer function.

One can improve over this simple model by considering individual halos (with individual mass and/or concentration), inferred from a learned model of the galaxy-halo connection, to assign dark matter density profiles based on observed galaxy properties. This results in a *non-linear* reconstruction method and is thus not captured by a transfer function. We explore this possibility by training a GNN model to infer the mass of NFW halos from the point cloud of galaxies, and then applying NFW profiles about the center of each inferred halo location. We compare this to an ‘exact’ version of this technique, where the density field is obtained by painting NFW profiles with parameters drawn from the true halo catalog of the simulation. We find that inferred halo masses somewhat degrade the reconstruction over assuming true (unobservable) halo masses.

A final comment regarding halo painting is that there is implicit dependence at the field level on how one assigns mass and the corresponding truncation radius of dark matter halos (e.g. at the virial radius, a density-dependent radius, etc); a related ambiguity is the total fraction of dark matter mass in halos that also host galaxies versus those that do not.

Point cloud-to-field level machine learning. In this paper, we further explore the performance of the combined GNN-CNN method from Ref. [41] to directly learn the non-linear galaxy point cloud-to-mass/baryon density field map. We train this architecture on the CAMELS suite of simulations, and compare the fidelity of the reconstruction to that obtained from the linear transfer function and halo painting methods described above. We demonstrate that this ML-based method yields the best reconstruction of the density fields among the methods we explore.

Relation to forward modeling. Many other works are concerned with forward modeling frameworks to connect matter to luminous matter. In forward modeling, one typically evolves *initial conditions* $\delta_{init}(\mathbf{x})$ to a final matter field by a deterministic forward model $\mathcal{F}(\Lambda_F)$ (such as a gravitational N-body simulation) which depends on unknown *forward model parameters* Λ_F (such as the matter density parameter Ω_M):

$$\delta_m(\mathbf{x}, t) = \mathcal{F}(\delta_{init}(\mathbf{x}), \mathbf{x}, t, \Lambda_F). \quad (2.8)$$

The small-scale galaxy distribution is often modeled in a second stochastic step, which samples the observable galaxies from the deterministic matter distribution:

$$\mathcal{P}_g(\delta_g^{\text{obs}}(\mathbf{x}, t) | \delta_m(\mathbf{x}, t), \Lambda_g). \quad (2.9)$$

Here Λ_g are the astrophysical parameters of the stochastic galaxy model. By assuming Gaussian initial conditions one can then sample the posterior

$$\mathcal{P}(\Lambda_F, \Lambda_g, \delta_{init} | \delta_g^{\text{obs}}) \quad (2.10)$$

which implies a reconstruction of $\delta_m(\mathbf{x}, t)$ through Eq. (2.8). The forward model for the galaxy distribution $\delta_m \rightarrow \delta_g$, whether stochastic or deterministic, is the inverse of our reconstruction which goes $\delta_g \rightarrow \delta_m$. There are many models for $\delta_m \rightarrow \delta_g$ in the literature, working at different scales, some examples including [51, 52]. However, forward modeling is more computationally expensive than the direct estimate we are making here, and it is not clear whether these more complicated methods outperform direct reconstruction. Further, forward modeling the matter distribution is only practical on sufficiently large-scales.

3 Simulation Data

3.1 Dataset

In this work, we use the CAMELS IllustrisTNG-CV simulation suite [42–44]. From this, we consider redshift $z = 0$ snapshots and the FOF-SUBFIND sub-halo/galaxy catalogs. The simulations evolve 256^3 dark matter and 256^3 gas particles in a $25 \text{ Mpc}/h$ box. This suite contains 27 simulations that differ by initial random seed, but have fixed cosmological parameters.

To make the galaxy catalogs closer to observable catalogs, we apply the selection criteria of Ref. [53]:

- The stellar and dark matter half-mass radii are greater than two Plummer radii ($R_p = 0.74 \text{ kpc}$).
- There must be more than 200 stellar and dark matter particles.
- Assume each sub-halo is a separate galaxy.

This leaves, on average, 283 galaxies in a $25^3 (\text{Mpc}/h)^3$ volume. The galaxy dataset is not fully realistic, but can broadly be compared to data from ongoing and future high number density photometric surveys. For instance, the number density of galaxies in our dataset is around 10 times larger than DESI at $z = 1$, but below the expected value from Rubin Observatory [54, 55].

To compare the performance of ML or traditional methods to reconstruct the dark matter field, we need a true dark matter 3D grid for comparison. In hydrodynamical simulations, each particle represents the volume of the Voronoi cell. So unlike in dark matter only N-body simulations, it does not make sense to use counts-in-cells (CIC) to assign the density to a grid. We instead use the CAMELS Multifield Dataset (CMD) [42, 45], which approximates the Voronoi cell by taking the radius to the 32nd nearest particle and assigning density to the grid based on the particles within that radius. We use the 256^3 resolution. For these CMD grids, 3 of the 27 simulations do not match the galaxy catalogs, so we only use 24 simulations¹. To summarize, we use the following data:

Input: Observed galaxy point cloud. We define galaxies as sub-halos of the gas particles in the CAMELS simulation. A galaxy is located at the position of the center of the sub-halo. Additionally, each galaxy is associated with a stellar mass, given by the number of stellar particles in the sub-halo, among other properties including r , g , z magnitudes, velocity dispersion, and stellar half-mass radius.

Output: Dark matter and baryon fields on a regular grid. Our target fields will be the unobserved dark matter and baryon density, generated by assigning particles to a regular grid. The precise grid-assignment procedure influences the field distributions on small-scales. As discussed above, we do not use the common CIC procedure for grid assignment, but rather a Voronoi volume inspired method, which is more appropriate for hydrodynamic simulations. In our analysis, this assignment is part of our definition of the ‘true’ fields.

¹We confirmed with the author of Ref. [45] that the 24 CMD simulations we use do correspond to the galaxy catalogs.

3.2 Visualizing the Data

To describe the halos in the simulations, we use the spherical overdensity halo mass M_{200} . This is defined as the total mass enclosed within a sphere, where the average density is 200 times the critical density of the universe. Formally, it is given by $M_{\Delta} \equiv (4/3)\pi r_{\Delta}^3 \rho_c \Delta$ where $\Delta = 200$, $\rho_c(z) = 3H^2(z)/8\pi G$ is the critical density, and $H(z)$ is the Hubble parameter. In Fig. (1) is the distribution of halo masses and r_{200} radii, averaged over all 27 simulations, for halos that host a central galaxy. The halo masses are plotted as the number density per logarithmic mass so that they can be compared to the halo mass function. Note that the drop-off at small halo masses is due to our selection criteria of including only halos with a central galaxy, e.g. we show $\langle N_{\text{cent}}(M) \rangle dn/dV/d\log_{10} M$ where $\langle N_{\text{cent}} \rangle$ is the mean number of centrals as a function of halo mass.

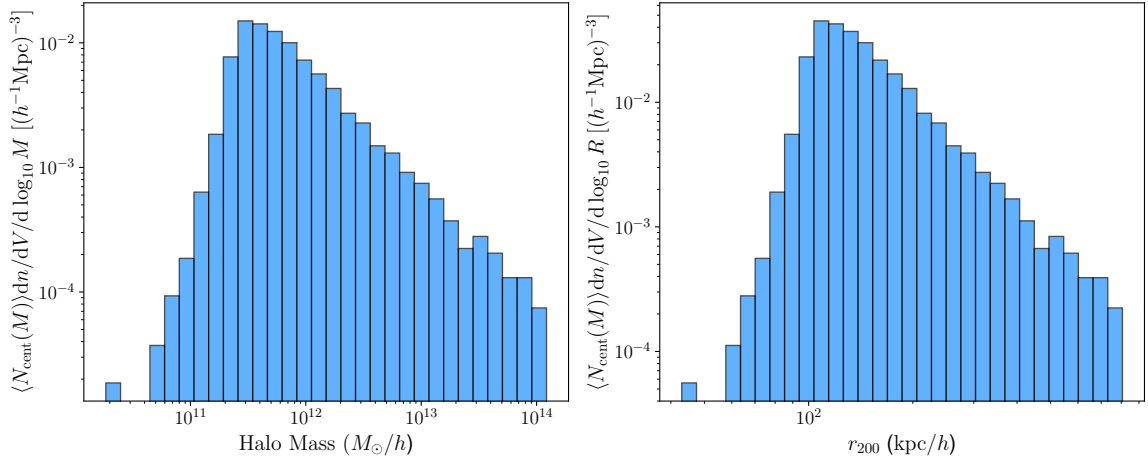


Figure 1: The probability of a halo hosting a central galaxy times the average number density distribution of halo masses (left) and r_{200} radii (right).

Across all the CV simulations, with our selection cuts, the average fraction of dark matter mass inside halos is 79% whereas for gas it is 36%. For this calculation, we defined the halo by its r_{200} radius. This demonstrates that the halo contribution is larger than the field contribution for dark matter, but the opposite applies for gas. The gas is much more dispersed outside of the halo. Therefore, for gas, it is more crucial to use field-based methods to construct the 3D density grid.

We aim to use galaxies to predict the underlying dark matter field. To get a better sense of the galaxy-dark matter connection in our simulation suite, we plot the cross-correlation power spectra in Fig. (2). Here, the dark matter density field was constructed using CMD to grid the dark matter particles. The galaxy density field was obtained through CIC, by weighting galaxies by their stellar mass. On large-scales the $P_g(k)$ and $P_m(k)$ are related by linear galaxy bias, but the correlation decreases towards smaller scales which are influenced by baryonic effects and non-linear gravitational evolution.

To better understand the setup, it is useful to visualize the corresponding locations of the observed galaxy cloud, dark matter halos, and the dark matter and gas fields. Figs. (3) and (4) depict the galaxy catalog after the selection cuts have been applied (red dots), the corresponding dark matter halos (depicted as spheres of r_{200} radius), and the dark matter and gas densities. Fig. (3) shows the $(25 \text{ Mpc}/h)^3$ volume, and Fig. (4) illustrates the zoomed-in

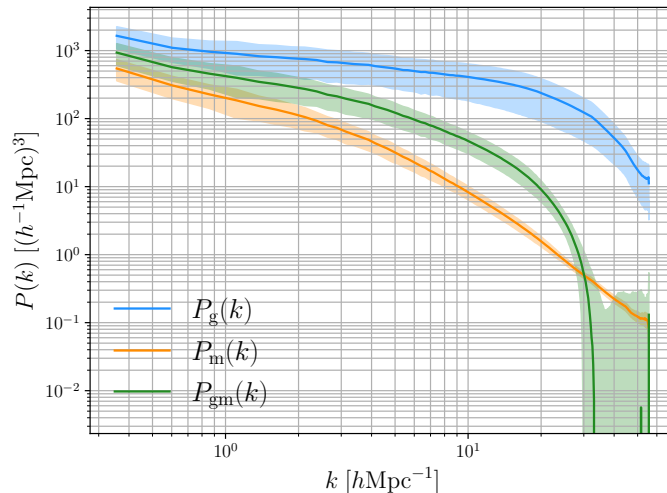


Figure 2: The auto-power spectra of the galaxy (blue) and dark matter (orange) fields. In green is their cross-correlation.

region around the largest halo. To visualize dark matter and gas densities, we plot the locations of each 50th particle of the corresponding type. We can make a few useful observations. The locations of the galaxies provide a better guess of the underlying density field distribution than just dark matter halos. We also notice that the gas distribution is spatially more spread out, while the dark matter is more clumped.

4 Methods

We consider different ML and non-ML methods to construct the continuous dark matter density field from a galaxy catalog. The non-ML benchmarks include using the CIC stellar mass-weighted galaxy field as a biased tracer of the dark matter field, constructing the dark matter field by applying a linear transfer function to the galaxy field, and painting the halo’s NFW profile onto a grid.

The first ML approach uses a GNN to predict halo mass from galaxy input features, which allows us to paint on the NFW profiles while accounting for the fact that halo mass is not directly observable. The next method, called GNN-CNN, treats the galaxies as a point cloud, assigning them to graphs which encode the information into a proto-density field, which is then passed through a CNN. These approaches are outlined below. By comparing with the linear baseline, we will examine whether non-linear methods have an advantage.

4.1 Performance Metric

To compare the performance of different methods, the most common metric is the *cross-correlation coefficient* of the reconstructed field $\hat{\delta}$ and the true field δ . In terms of the power spectra it is given by

$$r^2(k) = \frac{\langle P_{\text{true}}(k) \hat{P}(k) \rangle^2}{\langle P_{\text{true}}(k)^2 \rangle \langle \hat{P}(k)^2 \rangle} \quad (4.1)$$

where $P_{\text{true}}(k)$ is the power spectrum of the field and $\hat{P}(k)$ is the power spectrum of the estimate of that field. The cross-correlation coefficient is the relevant performance metric if

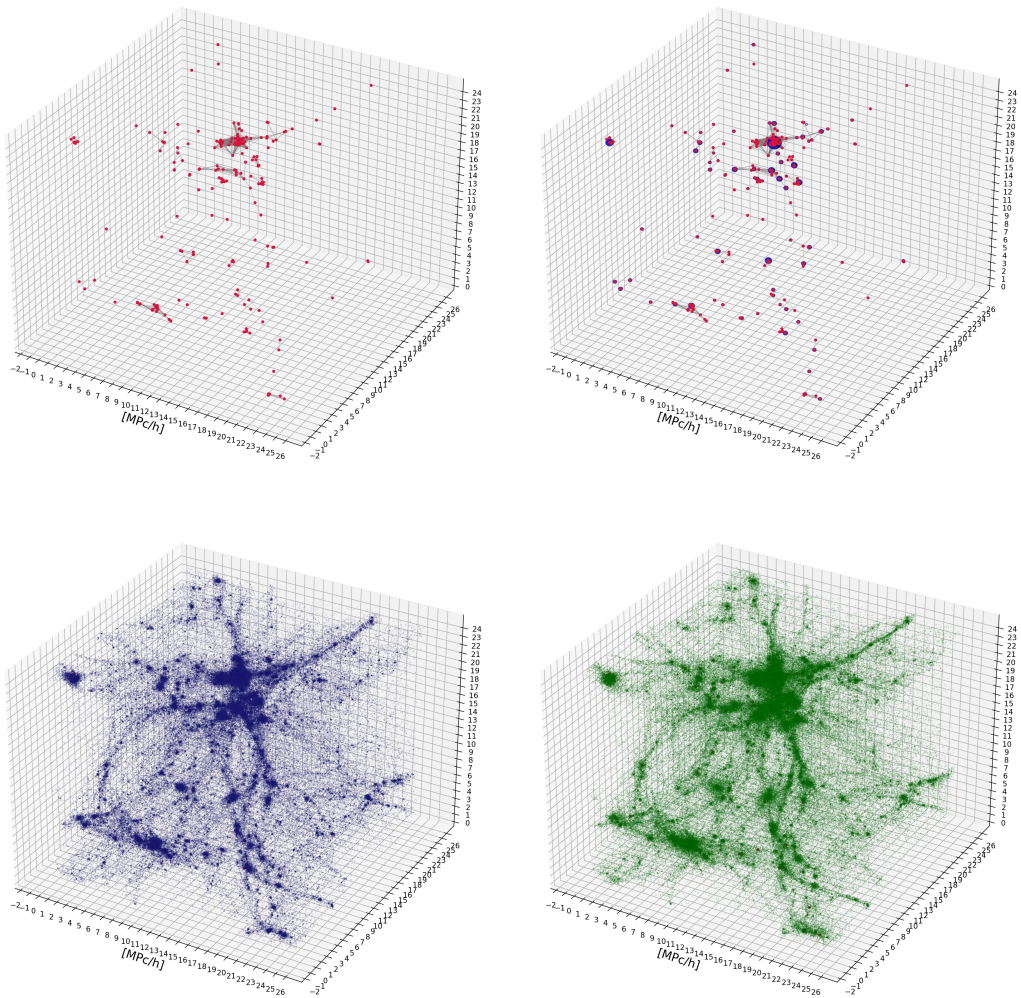


Figure 3: The distribution of galaxies (red points), dark matter halos (blue spheres), dark matter (blue) particles, and gas (green) particles in the simulation volume of 25^3 (Mpc/h)^3 . The radii of the spheres are proportional to r_{200} of the halo.

the goal is to increase the signal-to-noise ratio of a cross-correlation-based data analysis. We compute the power spectra using `Pylians` [56]. We do not deconvolve the window functions when plotting the power spectra, since they cannot be removed for the CMD fields. This means that there is a suppression of power at small-scales in the spectra plots.

4.2 Baseline: Simple Grid Assignment and Linear Transfer Function

As our baseline method, we use the mass-weighted tracer density. We thus assign the (stellar) mass-weighted galaxy point cloud to a regular grid, using the CIC procedure. We call the resulting field $\delta_g(\mathbf{k})$. We chose to mass-weight galaxies in the baseline because the shot noise would be quite large in the small Quijote volume otherwise, even though galaxy masses are only approximately observable.

The second baseline approach is using a linear transfer function. This is done by applying

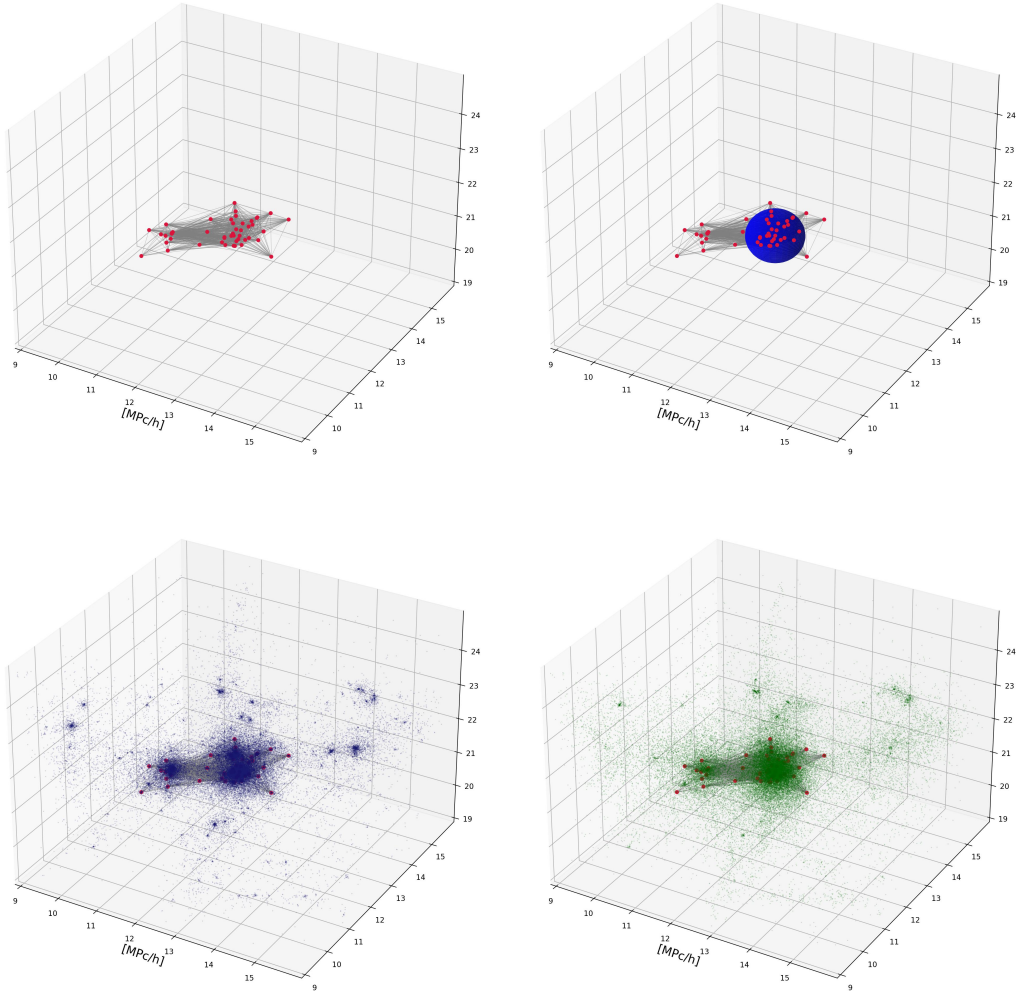


Figure 4: The distribution of galaxies (red dots) that belong to the largest halo in a simulation box. The halo is depicted as a blue sphere. Bottom left and right plots show the distribution of the dark matter and gas particles in the same zoomed-in region (blue and green correspondingly).

a linear kernel to the mass-weighted galaxy overdensity field ($\delta_g(\vec{x})$) in k -space:

$$\delta_m(\vec{k}) = \frac{P_{gm}(k)}{P_{gg}(k)} \delta_g(\vec{k}), \quad (4.2)$$

then Fourier transforming back to real space to get the dark matter overdensity field ($\delta_m(\vec{x})$). The $P_{gm}(k)$ and $P_{gg}(k)$ are calculated using the CIC mass-weighted galaxy field and the CMD true dark matter field. The linear transfer function can give a dark matter density field whose power spectrum is a good approximation to the true one, but the field-level residuals when compared with the true underlying dark matter field can be large.

The CIC and linear transfer function methods will have the same cross-correlation coefficient, because they both are using the galaxy field as a tracer of the dark matter field. However, the density fields will differ in real space, having different residuals when compared

to the true dark matter density. The benefit to considering both of these methods is that the linear transfer function is a fully linear approach so it can best demonstrate if there is a need for non-linear methods such as ML.

4.3 NFW Painting of Individual Halo Profiles

Another non-ML approach we consider is painting on NFW profiles using the true halo masses and radii. However, this approach requires known halo parameters and so cannot be applied directly to data without further inference of these parameters.

The NFW painting is done in Fourier space, which allows us to paint on the profile using the exact halo coordinates. The NFW density profile is given by

$$\rho(r) = \frac{\rho_s}{(r/r_s)(1 + r/r_s)^2} \quad (4.3)$$

where r_s is the scale radius which is set by the radius at which $n_{\text{eff}} = d\ln\rho/d\ln(r/r_s) = -2$. This can be related to the spherical overdensity definition through the halo concentration $c_\Delta \equiv r_\Delta/r_s$. We use a fit for the concentration parameter from Ref. [57] given by

$$c_{200} = 4.61 \left[\left(\frac{M_{200}/M_*}{638.65} \right)^{-0.07} \left(1 + \frac{M_{200}/M_*}{638.65} \right)^{0.07} - 1 \right] + 3.59 \quad (4.4)$$

where $M_* = 10^{12.5}$. The scale density is given in terms of the spherical overdensity parameters as

$$\rho_s = \frac{M_{200}c_{200}^3}{4\pi r_{200}^3} \frac{1}{\ln(1 + c_{200}) - (c_{200}/(1 + c_{200}))}. \quad (4.5)$$

This is fed into the analytic expression for the Fourier transform of the NFW profile [2]

$$u(k) = 4\pi\rho_s r_s^3 \left\{ \sin(kr_s) [\text{Si}([1 + c]kr_s) - \text{Si}(kr_s)] - \frac{\sin(ckr_s)}{(1 + c)kr_s} + \cos(kr_s) [\text{Ci}([1 + c]kr_s) - \text{Ci}(kr_s)] \right\}. \quad (4.6)$$

We define a Fourier-space grid with $k_{x,y,z} = \frac{2\pi}{L}n$ where L is the box size, N is the number of grid points per dimension (256), and $n = (0, 1, \dots, N/2, -N/2 + 1, \dots, -1)$. The total wavenumber is $k = \sqrt{k_x^2 + k_y^2 + k_z^2}$. To prevent aliasing, we need to account for the finite cellsize (L/N) by convolving with the Fourier transform of the cubic voxel (the 3D sinc function):

$$\tilde{\rho}(k) = \rho(k) \text{sinc}\left(\frac{k_x L}{N}\right) \text{sinc}\left(\frac{k_y L}{N}\right) \text{sinc}\left(\frac{k_z L}{N}\right). \quad (4.7)$$

We then apply a phase shift to center the halo

$$\hat{\rho}(k) = \tilde{\rho}(k) e^{-i(k_x x_h + k_y y_h + k_z z_h)} \quad (4.8)$$

where (x_h, y_h, z_h) are the halo's physical coordinates. Finally, we inverse Fourier transform to obtain the real space density

$$\rho(x, y, z) = \mathcal{F}^{-1}[\hat{\rho}(k)]. \quad (4.9)$$

A mask is applied to the field to ensure that all dark matter outside of the halo’s r_{200} radius is zeroed out. For $r_{200} < \text{cellsize}$, the mask leaves the dark matter in only that cell, to avoid completely zeroing out subgrid halos.

We compare our results to the true CMD density fields. We consider not just the complete dark matter fields, but also the true field with a mask applied to remove any dark matter outside of the halo’s r_{200} radius (ie. the halo field).

4.4 Halo-Level Machine Learning: GNN–NFW Painting

This is a ML extension to the NFW painting approach that predicts the halo masses of galaxy groups, allowing application to data.

4.4.1 Architecture

For the GNN part of this method, we use the public GNN code called `HaloGraphNet`² from Ref. [19], which used galaxy properties to infer the mass of halos. The architecture is fully explained in Ref. [19], but we summarize it below. The GNN uses message-passing, taking into account the edge (\mathbf{e}_{ij}) information through the EdgeNet set-up [58]:

$$1. \mathbf{e}'_{ij} \leftarrow \phi_e(\mathbf{w}_i, \mathbf{w}_j - \mathbf{w}_i, u) \qquad 2. \mathbf{w}'_i \leftarrow \max_{j \in \mathcal{N}_i} \mathbf{e}'_{ij}.$$

Here, the node features are \mathbf{w}_i and global features are u . The aggregation function is the maximum and ϕ_e is a MLP with three hidden layers alternated with two ReLU activation functions. The hidden layers respectively have 300, 300, and 100 hidden channels. We use only one message passing layer. To obtain a final graph-level representation, the network employs a combination of global sum, mean, and max pooling.

4.4.2 Training

We changed the `HaloGraphNet` code to have a different dataset format by creating a complex graph structure. This creates a graph for each halo which contains subgraphs corresponding to the galaxies within that halo. Each node is a galaxy, with the features:

- \vec{x} - Galaxy position
- r, g, z - Magnitudes of r,g, and z luminosity bands
- $r_{1/2}$ - Stellar half-mass radius
- M_* - Stellar mass
- σ_v - Velocity dispersion

Coordinates are normalized by the sidelength of the box. The stellar half-mass radius and velocity dispersion have a normalization factor applied and the stellar mass is kept in units of $10^{10} M_\odot / h$. The edges are constructed by linking all nodes within a radius of $2 \text{ Mpc}/h$. The global features are the total number of sub-halos and total stellar mass of the halo. Since we are training on simulations, we already know which galaxies belong to which halos. If this was extended to real data, the galaxies would need to be preprocessed using a group finder algorithm to determine their host halos. Another change from the `HaloGraphNet` code is that

²<https://github.com/PabloVD/HaloGraphNet>

we include halos with no satellite galaxies and apply different selection cuts as outlined in Section (3.1).

The target is the halo mass M_{200} and our dataset is at $z = 0$. We use an Adam optimizer with a learning rate 0.001 and a MSE loss

$$\text{MSE} = \frac{1}{N} \sum_{i=1}^N (\hat{f}_i - f_i^{\text{true}})^2 \quad (4.10)$$

where \hat{f} is the model output and f^{true} is M_{200} . We can use the full 27 CV simulations here for training and validation instead of only 24, since we train on the halo catalog not the CMD dark matter field. We use the first 18 for training and the last 9 for validation. The early stopping has a patience of 5 epochs and the minimum improvement in validation loss required to reset the patience counter is 0. The number of training epochs is 100 and the batch size is 4 for training, 1 for validation.

4.4.3 GNN-NFW Profile Painting

After the GNN provides M_{200} predictions, we then paint the dark matter density onto a grid using the NFW profile. This is the same procedure outlined in Section (4.3), but with predictions for the halo mass (and therefore the radius). Note that in this painting procedure, we use the true halo positions. If this was applied to real data the proxy could be the position of the central galaxy, which can be identified for instance by finding the brightest galaxy in the halo.

4.5 Field-Level Machine Learning: GNN-CNN Approach

4.5.1 Architecture

The GNN-CNN method of inferring the density distribution of dark matter we use here is a modification of the approach introduced in Ref. [41]. The original implementation consisted of a message-passing GNN block that encodes information from the galaxy feature inputs. Secondly, the GNN output was gridded using a learned grid assignment scheme to create proto-density fields. Lastly, this went into a CNN which acts as the decoder, outputting the density field prediction. In this work, we replaced the learnable grid assignment scheme with the standard CIC procedure for computational simplicity. It resulted in a negligible decrease of the reconstruction quality.

4.5.2 Training

The training dataset is prepared from CAMELS-IllustrisTNG-CV hydrodynamical simulations set as described in Section (3.1). Out of 24 simulations, we reserve 9 for validation and train our model on the rest. The input data are galaxy features which are the same set listed in Section (4.4.2). We normalize coordinates by the length of the box and they vary in the unit range. The magnitudes of the luminosity bands are normalized to have zero mean and unit variance. All other features - stellar mass, stellar half-mass radius, and velocity dispersion - are log-normalized, so that \log_{10} of the corresponding quantity has zero mean and variance of one. Scalar features correspond to the graph nodes (e.g. stellar mass), and the translationally invariant graph edges correspond to pairwise differences of vector features (e.g. position). The target is the dark matter and electron overdensities ρ_m , ρ_e , on a grid of 256^3 pixels. We scale them to have unit variance and zero mean. The neural network is

trained to minimize pixelwise l_2 loss with the AdamW optimizer. We set the initial learning rate to 8×10^{-4} and train the model for 100 epochs with the batch size of 1, saving the model with the lowest validation loss and reducing the learning rate by a factor of 3 if the validation loss does not improve for 10 consecutive epochs. The model is trained in mixed precision on a single RTX-3090.

5 Results: Dark Matter Reconstruction

5.1 Summary of Results

Before going over the results for each of these methods, we provide an overview of their performance. In Fig. (5), a slice of the density field is shown for each method. The left column is the true dark matter field (top) and the true halo field (bottom). The latter is defined as only the dark matter within the radius of the halo that encloses 200 times the critical density (r_{200}). Methods in the top row reproduce the dark matter field, but in the bottom row they either construct the halo field (NFW field) or the galaxy field as a biased tracer of the halos (mass-weighted field). A limitation of all these methods is their reliance on discrete tracers, meaning many areas of the cosmic web cannot be reconstructed. However, these regions are less crucial because the density is much lower, the log-scale of the plots artificially amplifies their significance.

Quantitatively, when compared to the true dark matter field, as shown by the cross-correlation coefficients in Fig. (6), the GNN-CNN consistently achieves the best performance, demonstrating improved correlation across all scales. Both the linear transfer function and the mass-weighted field (our baseline method, which grids the stellar density at observed galaxy locations) have the same cross-correlation coefficient with the true dark matter field. While the NFW field effectively paints on density profiles at halo locations and performs well at reproducing the halo field, it does not perform as well as the other methods when reconstructing the full dark matter field. The mass-weighted and linear transfer function fields account for dark matter dispersed outside of halos by also using sub-halo locations, so they do better than the NFW approach at reconstructing the full dark matter distribution.

We also reconstruct the gas field, which is shown in Section (6). The GNN-CNN again had the best reconstruction. We did not consider more cases in this work, but any field given by the simulations could be learned by the GNN-CNN architecture.

5.2 Baseline: Linear Transfer Function

The linear transfer function method results in the same cross-correlation coefficient as the galaxy mass-weighted field, as shown in Fig. (6). The power spectrum from the linear transfer function matches the true dark matter field spectrum until large k . A log-scale slice of the density field is illustrated in Fig. (5). The linear transfer function paints on the density to larger radii while the mass-weighted field are higher density in smaller regions. The linear transfer function field does not capture the small-scale structure as well as the non-linear technique of the GNN-CNN method as we will see below.

5.3 NFW Painting of Individual Halo Profiles

The NFW method paints on halo profiles, so it reproduces the halo power spectrum (over a restricted range of halo masses) rather than the full dark matter power spectrum. To make an accurate comparison of the NFW field to the true dark matter field, we mask the latter

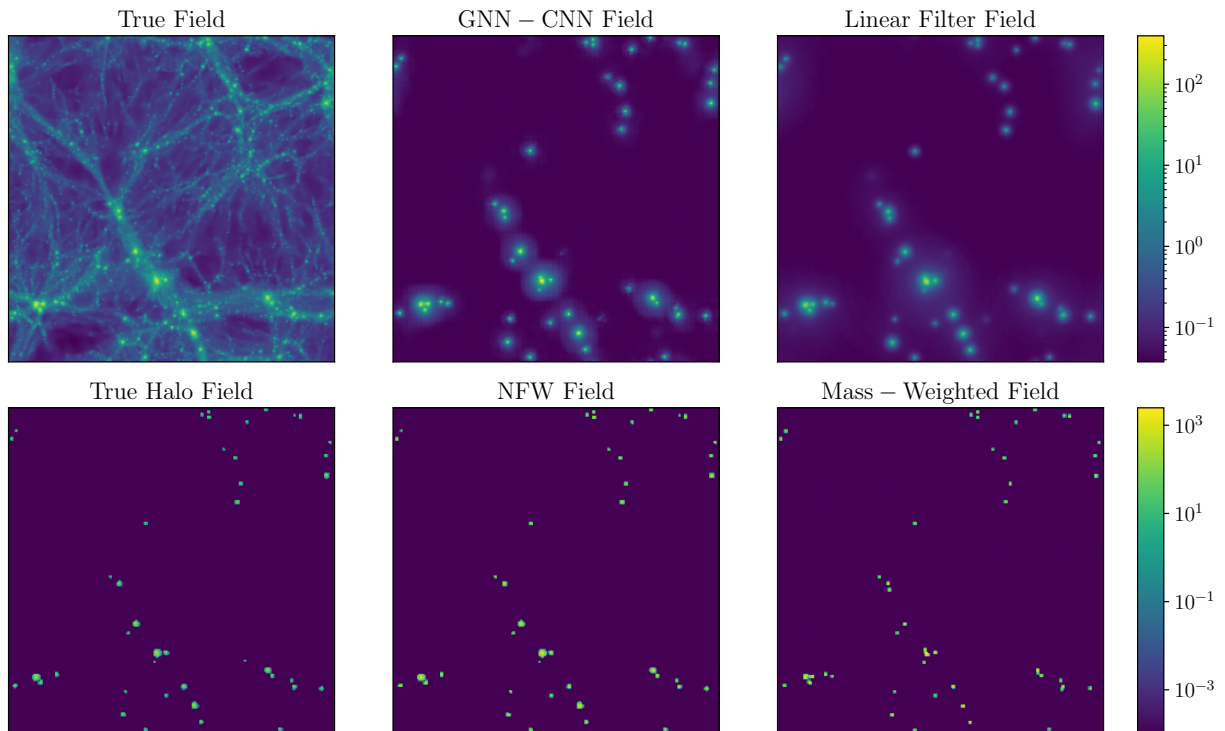


Figure 5: The top row show methods that reproduce the dark matter field and the bottom row shows either the halo or galaxy field. Top row: truth (left), GNN-CNN (middle) and linear filter (right) dark matter density fields. Bottom row: true halo (left), NFW (middle), and mass-weighted density fields. The fields are $1+\text{overdensity}$, plotted in a $5 \times 25 \times 25 \text{ (Mpc/h)}^3$ volume, averaged over the x axis. The colorbar is logarithmic with values clipped to 10^{-4} .

to only include regions inside of halos. Fig. (7) compares both the NFW painted field and the mass-weighted fields to the masked true halo field. The left panel shows the correlation coefficients. It is clear that the NFW field outperforms the mass-weighted field on all scales, even achieving perfect correlation at large-scales ($r(k) = 1$ at low k). In the right panel of the figure, we compare the power spectra. By masking the true dark matter field, we now have a true halo field $P(k)$, but it has a different amplitude because masking removes matter. To account for this, we have rescaled the $P_{\text{halo}}(k)$ to match $P_{\text{NFW}}(k)$ at low k . After rescaling, the power spectra match well down to small-scales.

Next, we tested how NFW painting performs compared to the full dark matter field, not just the halo component. As shown in Fig. (6), for small-intermediate k the NFW field is less correlated with the truth than performing CIC on the galaxy stellar masses. The right panel depicts the power spectra. Since the NFW field is discrete, it does not have the same shape as the dark matter power spectrum, and they are offset on large-scales by the halo bias.

A realspace comparison can provide a better picture of how the fields differ. In Fig. (5) is a zoomed-in log-scale slice of the density fields. In the bottom row, we see that the true halo field looks similar to the NFW painted field. The NFW painted field has placed spherical density profiles over the halos that extend to r_{200} . These profiles extend farther out than the mass-weighted field. Another difference is that the mass-weighted field is painting on the location of each of the galaxies in our catalog, instead of on the location of halos. The NFW

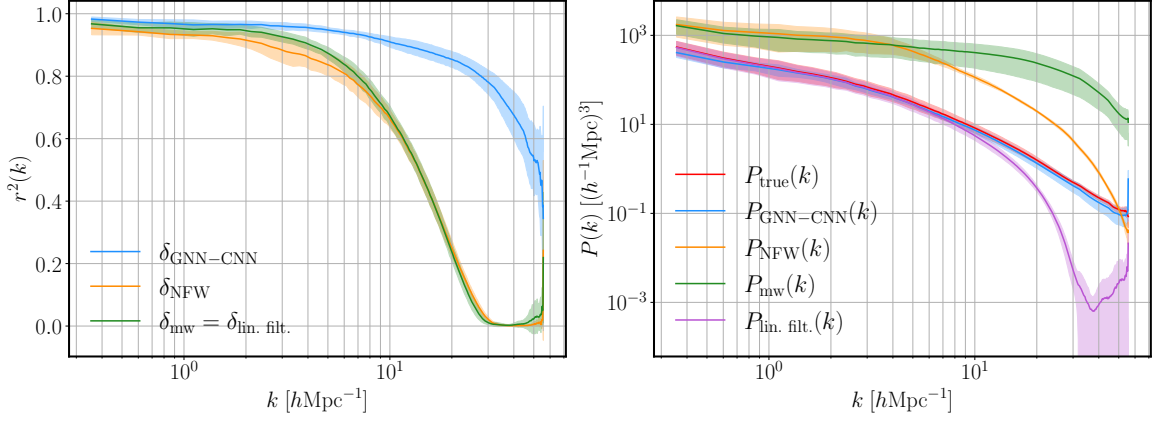


Figure 6: Left: The cross-correlation coefficients between the true dark matter density field and reconstructed fields. The reconstructed fields are the GNN-CNN (blue), NFW (orange), and galaxy mass-weighted/linear filter (green) fields. Right: The power spectrum of the true dark matter field (red) compared to GNN-CNN (blue), NFW (orange), galaxy mass-weighted (green) and linear filter (purple) fields. The NFW (mass-weighted) field reproduces the halo (galaxy) $P(k)$ so it is related to $P_{\text{true}}(k)$ by the halo (galaxy) bias.

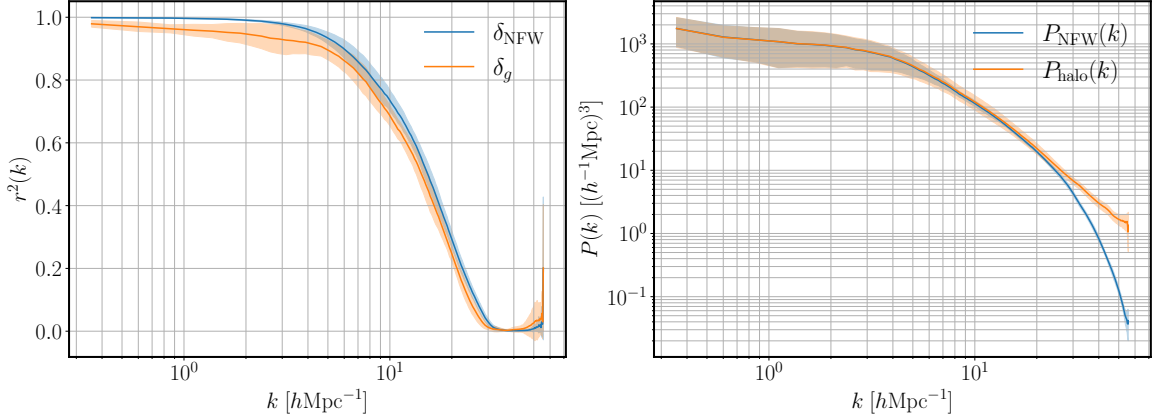


Figure 7: Left: The cross-correlation coefficients between the true halo field and the NFW painted dark matter density, δ_{NFW} (blue), and the galaxy mass field δ_g (orange). Right: The $P(k)$ of the true halo field (orange) and the $P(k)$ of the NFW density field (blue). $P_{\text{halo}}(k)$ is rescaled to match $P_{\text{GNN-NFW}}(k)$.

and mass-weighted fields conserve the mass of the simulation, while only painting on discrete objects. This results in halo densities that are higher than those seen in the true field. The top left image of the true full dark matter field shows filamentary structures that cannot be reproduced by the NFW or mass-weighted methods. To examine the difference in more detail, Fig. (8) is a zoomed in 2D projection of the true dark matter and NFW fields. The NFW field has red circles that show the r_{200} at which the density is cutoff.

A final check is how the NFW method changes with the galaxy number density, compared to the galaxy mass-weighted approach. When creating our galaxy catalog, one of the selection criteria we applied was that the number of stellar and dark matter particles (n_{part}) must be

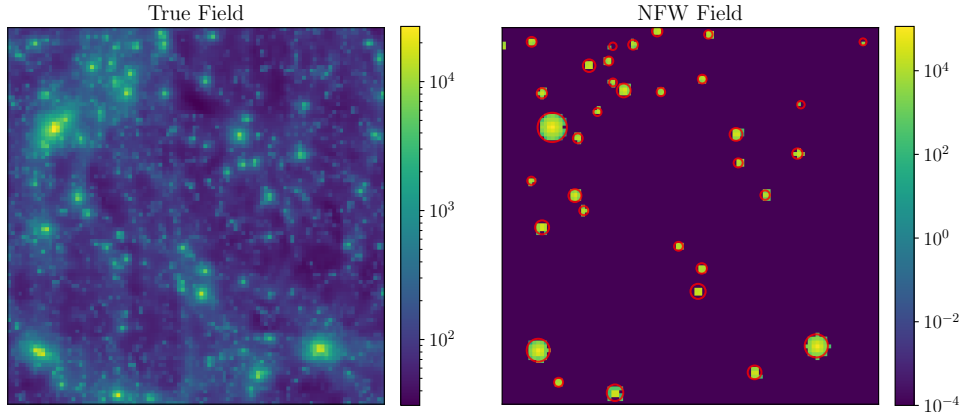


Figure 8: True (left) and predicted (right) NFW dark matter density, with red circles of r_{200} radius. The images are summed over the x-axis and zoomed in to a $10 \times 10 \text{ (Mpc/h)}^2$ region. These are plotted as $1 + \text{overdensity}$ and clipped to 10^{-4} for the logarithmic colorscale.

greater than 200, which resulted in an average of 283 galaxies in a simulation. We increased this threshold to $n_{\text{part}} > 800$ which changed the average number of galaxies to 136. This allows us to compare how these methods would perform on a galaxy survey with a lower number density of objects. As seen in the top panel of Fig. (9) for the NFW field and in the bottom panel for the galaxy mass-weighted field, the correlation coefficient decreases with the number density of galaxies. This is more pronounced for the NFW field. To enable a rough comparison of the power spectra, we scaled the true dark-matter power spectrum by the galaxy bias to approximate the halo clustering signal (i.e., the 2-halo term). However, this only provides a comparison at the lowest k . We used the galaxy bias from the $n_{\text{part}} > 200$ galaxy catalog. The mass-weighted field $P(k)$ does not match the true dark matter field because it is the galaxy power spectrum.

These results demonstrate that NFW painting can outperform the stellar mass-weighted approach if our goal is to reconstruct the halo field. If the goal is to reconstruct the full dark matter field, then mass-weighting is better. It is important to note that in practice we do not know the true halo parameter values, so this idealized scenario cannot be applied to real data. Furthermore, we used halos found from particles for the training dataset and use the true halo positions from the simulations. If this were done more realistically, we would use halos found from grouping galaxies and the central galaxy’s position as a proxy for the halo’s position. These changes would further lower the performance, suggesting that the NFW painting approach is suboptimal to a galaxy mass-weighted field. In light of this result, we do not extend a halo-painting approach to gas reconstruction.

5.4 Halo-Level Machine Learning: GNN-NFW

We now explore how the performance of halo painting is affected when a GNN is used to predict the halo properties used in the NFW profiles from galaxy features. Fig. (10) is a comparison of the outputs of the GNN model with the ground truth for M_{200} . The red

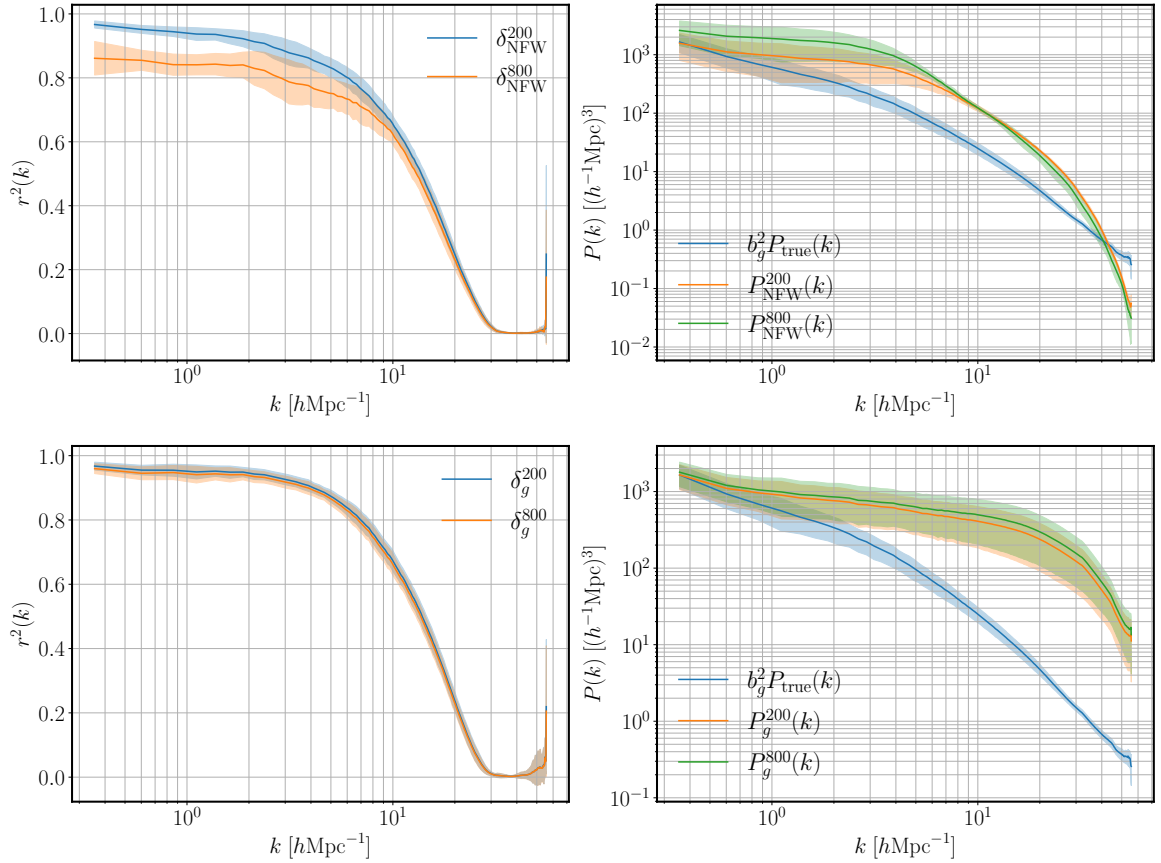


Figure 9: Left: The cross-correlation coefficient of the true dark matter density field with the NFW (top) or mass-weighted field (bottom). In blue are the results using the $n_{\text{part}} > 200$ selection cut and orange is $n_{\text{part}} > 800$. Right: The $P(k)$ of the true dark matter field rescaled by $b_g |_{n_{\text{part}} > 200}$ (blue). In the top image is the NFW painted density field $P(k)$ for $n_{\text{part}} > 200$ in orange and $n_{\text{part}} > 800$ in green. The bottom image has the same cases but for the mass-weighted field.

dashed line shows where the model outputs correspond exactly to the true values. From this we can see that the GNN performs well at intermediate M_{200} , but deviates more at the lowest and highest masses. This makes sense as there are fewer halos in these regions to train on, especially at the high-mass end. The model achieves a scatter of ~ 0.02 dex in $\log_{10}(M/(10^{10} M_{\odot}/h))$.

The top left panel of Fig. (11) shows the correlation coefficients of the true halo field with both the GNN-NFW painted field and the mass-weighted field. Across all scales, the true field correlates better with the $\delta_{\text{GNN-NFW}}$ field than the δ_g field. However, the GNN-NFW field has a lower cross-correlation coefficient than the NFW painted field shown in Section (5.3). This is to be expected since the GNN-NFW method accounts for our uncertainty in the halo masses. In the right panel, we see that the power spectrum aligns well with the true halo field until small-scales, but the NFW field had slightly better agreement at intermediate scales.

Fig. (11) compares GNN-NFW to the full dark matter field in the bottom panel. Overall, GNN-NFW has a similar performance as the NFW painted case (Fig. (6)). On large-scales,

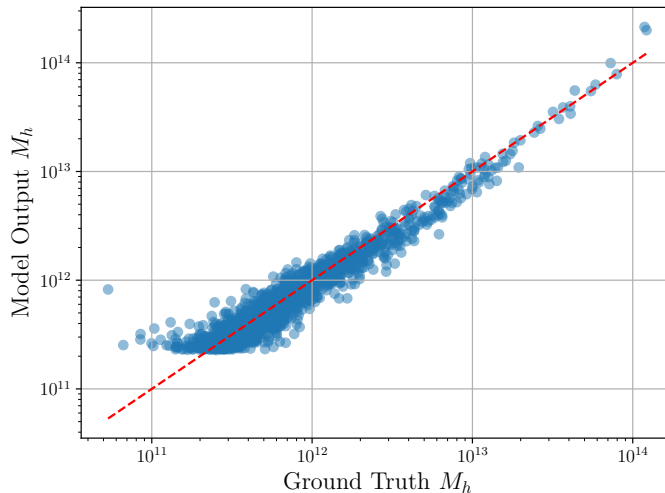


Figure 10: The GNN model output for halo mass compared to the true values. The red dashed line represents perfect correlation.

GNN-NFW shows slightly higher correlation, but this is likely coincidental, as both methods aim to reconstruct the halo field, not the full dark matter field. The GNN-NFW power spectrum also closely resembles the NFW result. Not depicted here is the GNN-NFW field in realspace since visually it has the same behaviour as the NFW field.

Overall, the results mirror what we saw for NFW painting, but this approach has some realism added to account for our uncertainty about the halo mass values. The conclusion is the same, that NFW painting based methods can improve upon stellar mass-weighting for the halo field, but not for the full dark matter field.

5.5 Field-Level Machine Learning: GNN-CNN

We show the cross correlation coefficient of the dark matter overdensity, reconstructed with the GNN-CNN setup (blue), and the mass-weighted galaxy field (green) with the true dark matter overdensity in Fig. (6) (left). The right plot shows the true and recovered power spectra. As can be seen, the method provides a high-quality and unbiased reconstruction up to the highest wave numbers, for example $r^2(k)|_{k=3 \text{ Mpc/h}} \approx 0.8$. It is also worthwhile to look at the reconstructed fields. Fig. (12) shows the true (left) and reconstructed (middle) δ_m along with the input galaxy catalog, visualized as a graph (right). We take a slice of the 3D field with a width of 5 Mpc/h and project it along the slice axis. We see that in the regions where we observe a lot of galaxies, the model provides a good reconstruction of the underlying dark matter field. The model struggles with more complex structures, like sheets and filaments. This is expected since there are not so many objects to learn from in such regions. We also show the reconstructed field in a more dense region in Fig. (13). To check the robustness of our method to the number density of observed galaxies, we repeat the training, imposing the particle number cut. In our default configuration, we required that each galaxy consists of at least 200 stellar particles. We now raise this requirement to 800 particles. This results in a reduction of the average number of galaxies per simulation from 283 to 136. The resulting power spectra and cross-correlation coefficients are shown in Fig. (14). We can see that the cross-correlation coefficient decreases slightly at higher k values. We also notice that

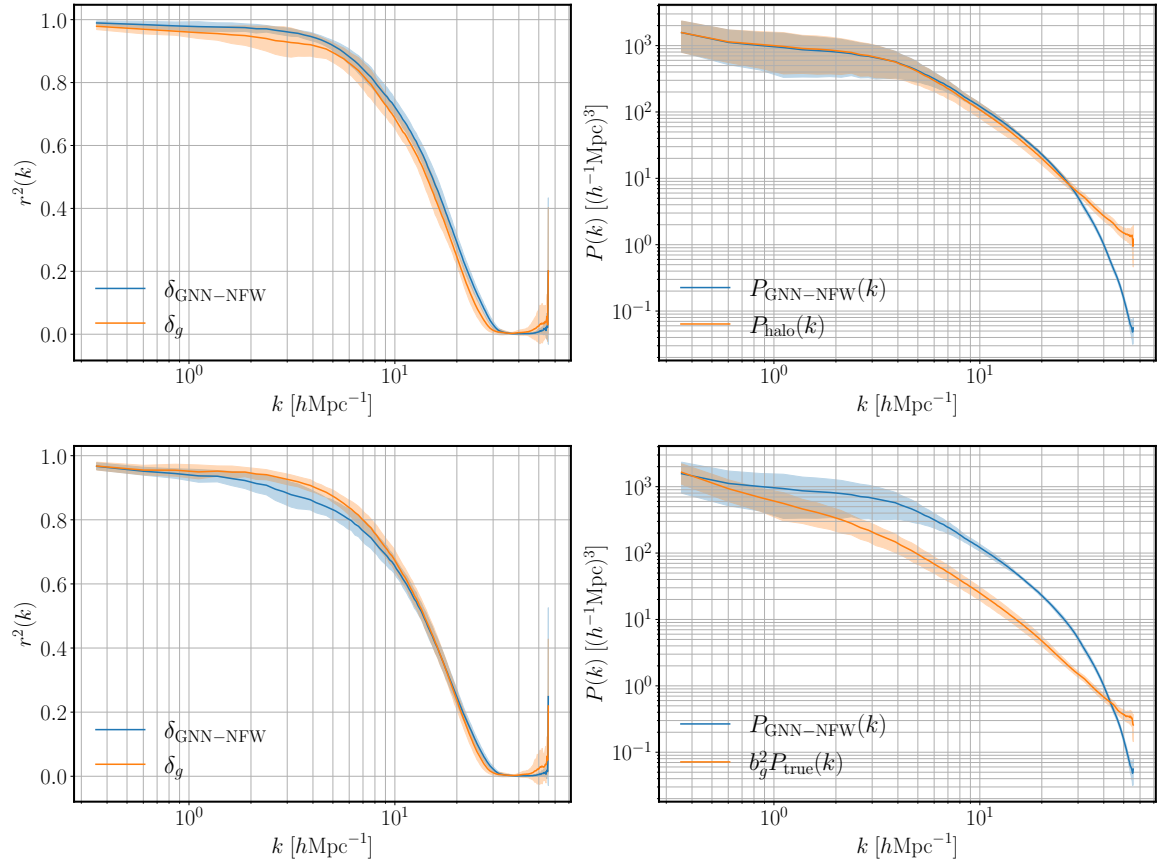


Figure 11: Left Top: The cross-correlation coefficient of the GNN-NFW painted dark matter density, δ_{NFW} (blue), and galaxy mass field δ_g (orange) with a true halo field. Right Top: The $P(k)$ of the true halo field (orange) and the $P(k)$ of the GNN-NFW reconstructed density field (blue). $P_{\text{halo}}(k)$ is rescaled to match $P_{\text{GNN-NFW}}(k)$. Bottom: Same images as the top, but for the true dark matter field. The true dark matter density’s $P(k)$ is rescaled by galaxy bias squared.

the reconstructed field with the higher particle number cut contains less power at all scales. It is natural to expect, since our method paints a dark matter field around each individual object, and fewer objects will result in lower variance on average.

6 Results: Gas Reconstruction

We now move on to describe the reconstruction of the gas field. For NFW/GNN-NFW painting, the results would be significantly worse than for dark matter, since gas is more diffuse, so less of it is located in the halo component of the gas field. Similarly for the mass-weighted field, galaxies will not capture the extended gas profiles. Therefore, we present only the gas results for the GNN-CNN and linear transfer function methods.

The cross-correlation coefficients in Fig. (15) demonstrate that the GNN-CNN outperforms the linear transfer function on all scales. Small-scales are significantly improved by using this ML approach, which can also be seen at the level of the power spectra in the right-hand panel of Fig. (15). At the field level, the two methods are similar, but the linear

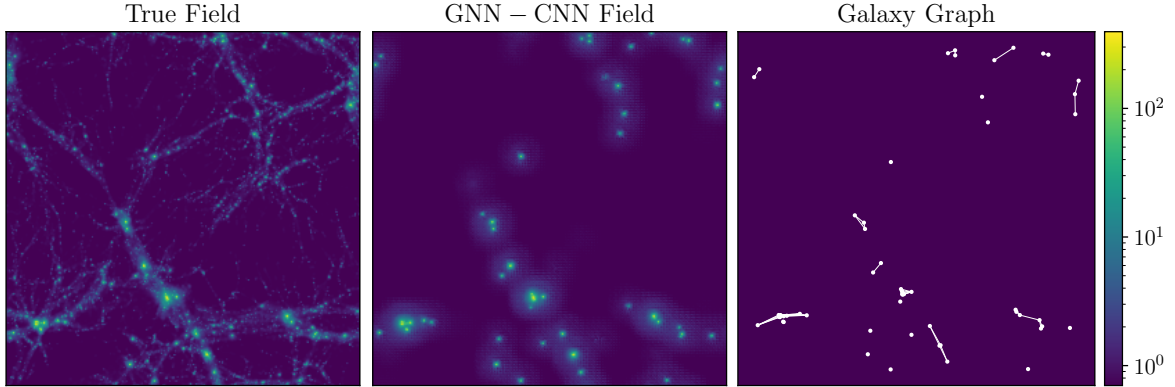


Figure 12: True (left) and predicted with GNN-CNN setup (middle) dark matter density in a $5 \times 25 \times 25$ (Mpc/h)³ volume, averaged over the x axis. The rightmost column shows the visualization of the input galaxy cloud, in the same region, as a graph.

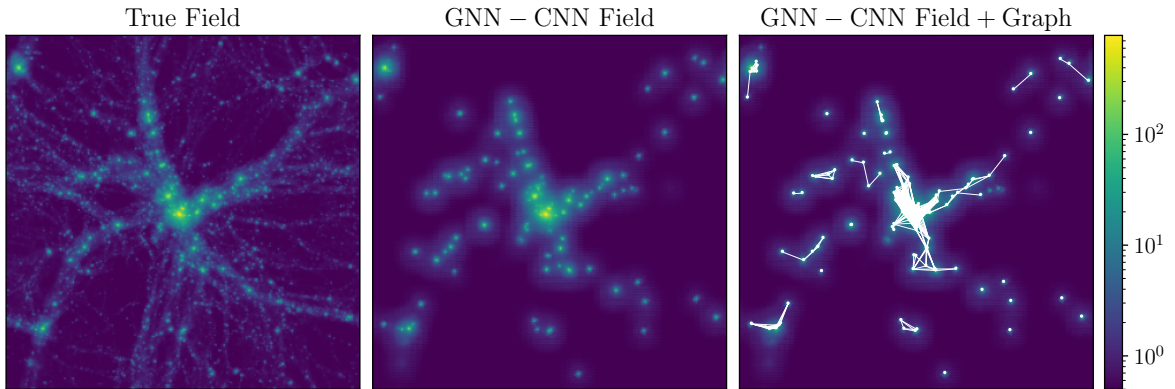


Figure 13: Example of the reconstructed dark matter density $\rho/\bar{\rho}$ (middle), in the $25 \times 25 \times 10$ (Mpc/h)³ volume, projected along the z axis. The right plot shows the overlaid input galaxy graph, and the plot on the left is the target density.

transfer function field is a bit more diffuse - as shown in Fig. (16). The true field image also illustrates how the majority of gas is outside halos, as opposed to dark matter (Fig. (5)), which highlights the importance of field-based reconstruction.

This result is important for kinetic Sunyaev-Zel'dovich (kSZ) velocity reconstruction [10, 59–70]. The kSZ effect is a cosmic microwave background (CMB) secondary anisotropy contribution from Thomson scattering of CMB photons by free electrons in bulk-motion [71]. It is proportional to the optical depth and velocity. To extract a velocity from the kSZ effect, a model for the optical depth is needed. Currently, the linear transfer function method is used to model the electrons from observed galaxies. Therefore, the small-scale improvement shown by the GNN-CNN could improve kSZ velocity reconstruction. This idea was introduced in [72], where it was shown that the velocity quadratic estimator noise is inversely proportional to the integrated cross-correlation coefficient of the template with the true electron field, so the improvement in $r^2(k)$ directly translates into the improvement in the velocity reconstruction. For this application, modeling uncertainties create a scale-independent bias (on large-scales) (eg. Refs. [10, 64, 73–75]) so this can absorb any bias from our training data differing from

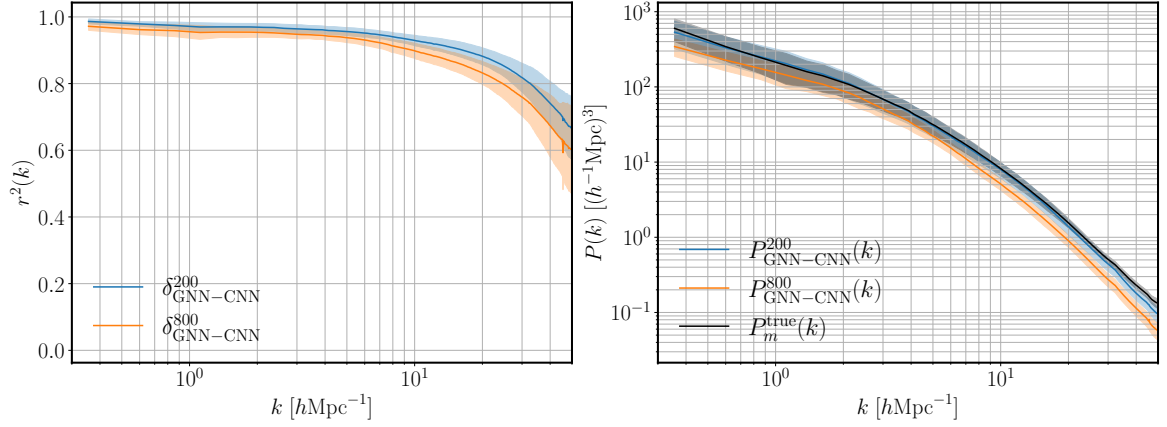


Figure 14: Cross correlation coefficients and power spectra of reconstructed dark matter density fields with GNN-CNNs trained on different number densities. Cut off of 200 particles per galaxy corresponds to 283 galaxies per volume on average (blue), while 800 particles results in 136 galaxies (orange).

real data.

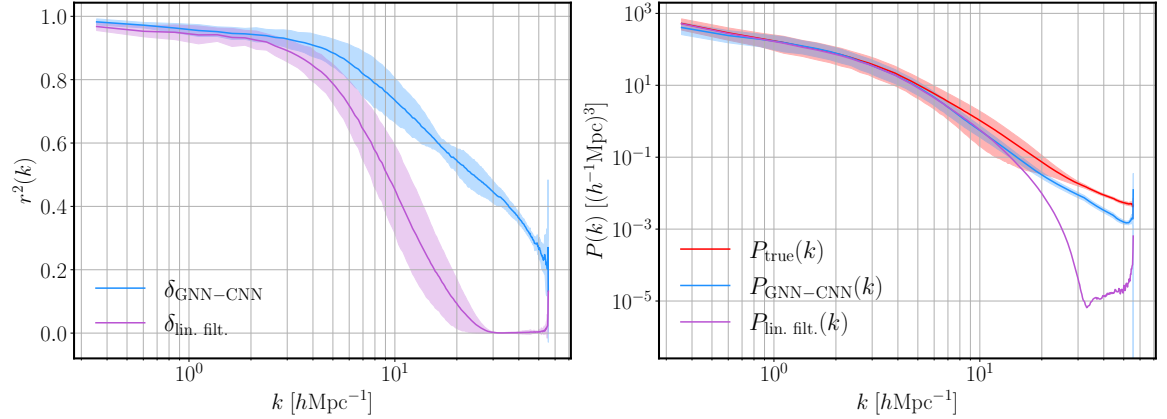


Figure 15: Left: The cross-correlation coefficients between the true gas density field and GNN-CNN (blue) and linear transfer function (purple) reconstructed fields. Right: The true gas field (red) compared to GNN-CNN (blue) and linear transfer function (purple) fields.

7 Robustness Against Unknown Feedback Parameters

We now discuss the robustness of the machine-learned dark matter field to changes in the astrophysical feedback parameters. In all previous discussions, the model was trained and tested on simulations from the same set with the same fiducial values of cosmological and astrophysical parameters. However, it is interesting to see how the model performs on a simulation that has significantly different fiducial parameter values. For this purpose, we use the EX subset of CAMELS-IllustrisTNG. This subset has 4 simulations, one with fiducial values and 3 with the values of the astrophysical parameters at their extremes. We consider three cases:

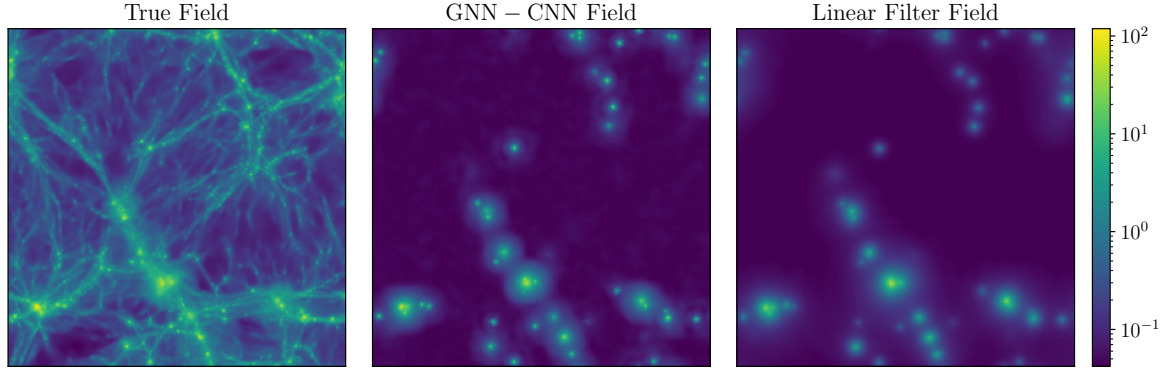


Figure 16: The 1+overdensity gas fields in a $5 \times 25 \times 25 \text{ (Mpc/h)}^3$ volume, averaged over the x axis. On the left is the truth, middle is the GNN-CNN and right is linear transfer function gas field. The colorbar is logarithmic with values clipped to 10^{-4} .

- Fiducial: 282 galaxies
- Efficient Active Galactic Nuclei (AGN) feedback: 284 galaxies
- No feedback: 1018 galaxies.

For this test, we again only evaluate the performance of GNN-CNN and linear transfer function methods. The GNN-CNN is trained on a subset of the CV simulations. For the linear transfer function, the ‘training’ step involves applying a filter (Eq. (2.2)) derived from one of the CV simulations to the EX simulations. In Fig. (17), the cross-correlation coefficients for the GNN-CNN and linear filter fields do not change significantly between the simulations. If there are errors with the individual halo profiles, these get diluted by averaging across all the halos in the simulation. So, even for the most extreme case where there is no feedback, the cross-correlation is not significantly impacted because there are so many halos.

To quantify how biased the results are, we plot $b(k) = P_{\text{rec} \times \text{true}}(k)/P_{\text{true}}(k)$ where $P_{\text{rec}}(k)$ is the GNN-CNN or linear transfer function result. This is shown in Fig. (18). For both the GNN-CNN and linear transfer function methods, the bias generally remains scale-independent. The main exception is the GNN-CNN no feedback reconstruction, which also exhibits the largest bias. This significant drop in performance for the no feedback case is likely due to the extreme change in galaxy number density; this simulation contains over three times the number of galaxies present in the training set. It is promising that the very efficient AGN simulation does not result in a significant bias. Additionally, we anticipate that the GNN-CNN’s performance could improve when applied to different simulations if trained (as in the initial paper [41]) on simulations with varying cosmological and astrophysical parameters.

8 Outlook: Using the Model for Parameter Inference

The purpose of our work is to make a template of unobserved fields for cross-correlation analyses, such as gravitational lensing (dark matter template) or kSZ tomography (gas template). The observed cross-correlation will be strongest if the cosmological and astrophysical parameters assumed by the neural network model match those of reality. If we train our model as a function of cosmological and astrophysical parameters Λ (a vector of parameters), we can thus use it for parameter inference.

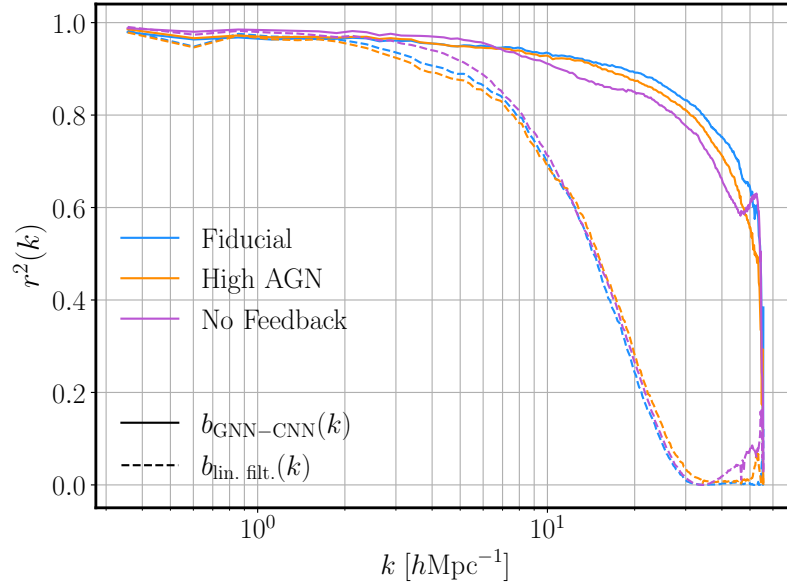


Figure 17: The cross-correlation coefficients of the truth with the GNN-CNN (straight) and linear transfer function (dashed) dark matter fields. The simulations are fiducial (blue), high AGN feedback (orange), and no feedback (purple).

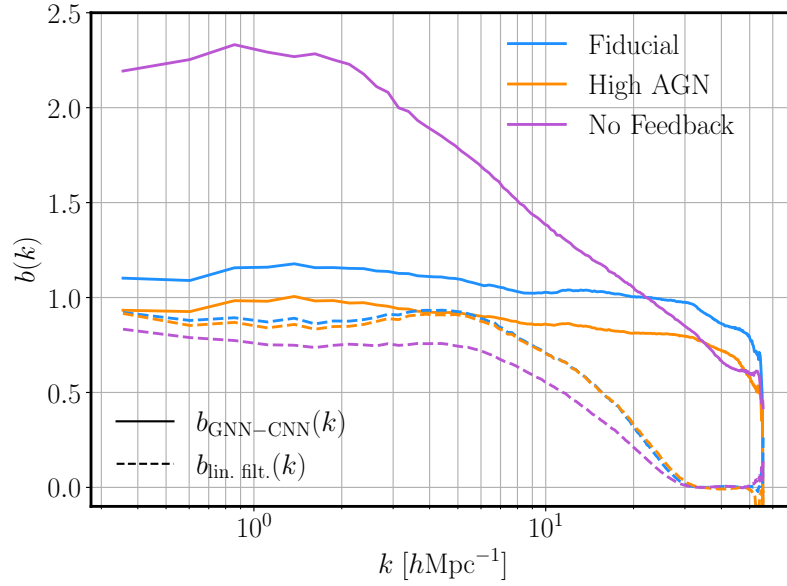


Figure 18: The bias of the reconstructed power spectra to the truth, for the GNN-CNN (straight) and linear transfer function (dashed) reconstructions. The simulations are fiducial (blue), high AGN feedback (orange), and no feedback (purple).

We outline how this works conceptually. Assume that we have trained the neural network

$$\hat{\delta}_m^{NN} = \text{NN}_{\theta}(\delta_g^{\text{obs}}, \Lambda), \quad (8.1)$$

from a data set that spans a range of these values Λ using a MSE loss

$$\mathcal{L}_{\text{train}}(\theta) = \mathbb{E}_{(\delta_g^{\text{obs}}, \Lambda, \delta_m) \sim \mathcal{D}} \left[\left\| \text{NN}_{\theta}(\delta_g^{\text{obs}}, \Lambda) - \delta_m \right\|_2^2 \right]. \quad (8.2)$$

We make the simplifying assumption that we have also measured the true dark matter density δ_m^{lens} directly from gravitational lensing (in reality, reconstructing the 3D matter distribution from lensing can only be done approximately). We are thus given a pair $(\delta_g^{\text{obs}}, \delta_m^{\text{lens}})$, but Λ in reality is unknown. We wish to estimate Λ such that the neural network prediction $\hat{\delta}_m = \text{NN}_{\theta}(\delta_g^{\text{obs}}, \Lambda)$ matches the known δ_m^{lens} . We do this by solving the following optimization problem:

$$\hat{\Lambda} = \arg \min_{\Lambda} \mathcal{L}_{\text{infer}}(\Lambda), \quad \text{where} \quad \mathcal{L}_{\text{infer}}(\Lambda) = \left\| \text{NN}_{\theta}(\delta_g^{\text{obs}}, \Lambda) - \delta_m^{\text{lens}} \right\|_2^2. \quad (8.3)$$

This can be done via gradient-based optimization (e.g., Adam) since our model is auto-differentiable. For simplicity, we have formulated the above optimization problem in terms of maximum likelihood, but it would be straight forward to generalize this to a Bayesian formulation including priors on the Λ parameters.

To obtain uncertainty on the estimated parameters $\hat{\Lambda}$, we use a Laplace approximation of the posterior $p(\Lambda \mid \delta_g^{\text{obs}}, \delta_m^{\text{lens}})$, assuming a locally Gaussian form around the optimum:

$$p(\Lambda \mid \delta_g^{\text{obs}}, \delta_m^{\text{lens}}) \approx \mathcal{N}(\hat{\Lambda}, \Sigma_{\Lambda}). \quad (8.4)$$

The covariance matrix is obtained from the Hessian at the optimal point

$$H = \nabla_{\Lambda}^2 \mathcal{L}_{\text{inv}}(\Lambda) \Big|_{\Lambda=\hat{\Lambda}} \Rightarrow \Sigma_{\Lambda} = H^{-1} \quad (8.5)$$

and provides the error bars on the parameters. For example, if a scalar parameter Λ_i has a small error bar $\sigma_{\Lambda_i} = (H^{-1/2})_{ii}$, that means that this parameter is well determined by the data. Conversely, if σ_{Λ_i} is large, it means that the reconstruction is not sensitive to this parameter (which can also be interpreted as the reconstruction being robust to this parameter).

Of course, whether one can make interesting measurements in this way depends on whether the training data are sufficiently realistic, i.e. whether it models small-scale physics sufficiently accurately rather than being dominated by systematic simulation uncertainties. It is not likely that interesting cosmology constraints can be obtained in this way; however, for small-scale astrophysics parameters, the model should give some insights, for example whether AGN feedback is small or large. Contrary to other methods, the approach described here is not based on computationally expensive sampling of a forward model (with a probabilistic dark matter to galaxy connection) and may thus be easier to perform in practice. Since it works at field level, in principle it has access to all information to the extent that the Gaussian approximations above hold in practice.

9 Conclusions and Outlook

In this paper, we compared different methods of reconstructing continuous fields, in particular dark matter, from discrete tracers. We compared linear transfer function methods (which includes painting uniform profiles on each object), individual halo painting (depending on the halo mass), and finally field-level machine learning. As a baseline, we used a simple stellar mass-weighted grid assignment of galaxies. Our findings are:

- Although the linear transfer function method has the same correlation coefficient with the true dark matter field as the unfiltered baseline (Fig. (6)), it is a better representation at the field level with smaller residuals (Fig. (5)).
- We find that reconstructing dark matter by painting individual spherical halos with mass-dependent NFW profiles increases the cross-correlation with the true dark matter distribution *within* the radius of the halo (Fig. (7)), but lowers the cross-correlation with the entire true dark matter field (Fig. (6)).
- While we find that a GNN can predict the mass of the host halo quite well (Fig. (10)), this does not translate into an improved reconstruction of the dark matter field compared to simple mass assignment of galaxies.
- We find that the non-linearity and expressiveness of the field-level neural network is helpful in improving the reconstruction. The GNN-CNN approach clearly outperforms simple grid assignment or halo model approaches (Fig. (6)). The cross-correlation coefficient shows improvement across all scales, notably extending to small-scales where, for instance, $r^2(k)|_{k=3 \text{ Mpc/h}} \approx 0.8$, a significant gain over other methods that had already dropped to zero.
- The GNN-CNN was the most effective method for reconstructing the gas field (Fig. (15)), underscoring the critical role of field-level methods given that gas largely resides outside of halos.
- We found the GNN-CNN to be fairly robust against astrophysical biases when applied to simulations with extremely different astrophysics than the training data (Fig. (17)). The linear transfer function proved to be more robust to extrapolating to simulations with varying astrophysics. However, we could further improve the GNN-CNN performance by training on a simulation suite with varying astrophysical and cosmological parameters.

Ultimately, the GNN-CNN ML approach delivered the best results, for dark matter and gas. This method correctly represents galaxies as point clouds and improves the reconstruction of small-scale details in the gridded field. The GNN-CNN notably improved the cross-correlation coefficient with the true field across all scales compared to our baseline, with the most significant improvements on small-scales.

It would be interesting to train our neural network method on existing and upcoming high-resolution large-volume simulations such as FLAMINGO [76] and MilleniumTNG [77]. Because they span a larger volume, one could construct a more realistic mock survey, including a survey mask. In this work, we chose to use CAMELS because this set includes simulations with different astrophysical and cosmological parameters. However, the small volume of CAMELS limits both the largest scales that we can probe and the range of cluster masses in the training data. To apply the method to real data, one would need to make a more realistic galaxy set, in redshift space and with galaxy features that include appropriate noise. Applying the method to a large survey volume would also require a convolutional or patch-wise implementation. We note, however, that no training simulation with the full survey volume is needed, since we aim to learn small-scale nonlinear physics only.

In summary, the GNN-CNN method showed a clear improvement over the linear filter technique, which is currently employed in applications such as large-scale velocity reconstruction with kSZ [10, 63–70] and searches for light bosons using resonant conversion [78–80]. This

indicates that adopting the GNN-CNN setup could increase the quality of these and similar analyses. More broadly, this technique’s ability to provide a field-level reconstruction of dark matter — the fundamental scaffolding of the universe’s matter content — makes it generally applicable to cross-correlation studies, with probes like cosmic shear, 21-cm intensity maps, fast radio bursts, and gravitational wave sources. We explore these and other applications in future work.

Acknowledgments We thank H. Ganjoo for discussions and collaboration on alternative architectures for reconstructing cosmological fields. We thank C. K. Jespersen for discussions on graph neural networks. We are grateful to Francisco Villaescusa-Navarro for the useful clarification about the CAMELS dataset. M.M. acknowledges the support by the U.S. Department of Energy, Office of Science, Office of High Energy Physics under Award Number DE-SC-0017647, and by the National Science Foundation (NSF) under Grant Number 2307109. M.C.J. is supported by the National Science and Engineering Research Council through a Discovery grant. J.K. acknowledges support from the Natural Sciences and Engineering Research Council of Canada (NSERC) through the Vanier Canada Graduate Scholarship. Y.K. and M.M. are grateful for the hospitality of Perimeter Institute, where a part of this work was done. Research at Perimeter Institute is supported in part by the Government of Canada through the Department of Innovation, Science and Economic Development Canada and by the Province of Ontario through the Ministry of Colleges and Universities.

References

- [1] N.-M. Nguyen, F. Schmidt, B. Tucci, M. Reinecke and A. Kostić, *How Much Information Can Be Extracted from Galaxy Clustering at the Field Level?*, *Phys. Rev. Lett.* **133** (2024) 221006 [[2403.03220](#)].
- [2] A. Cooray and R.K. Sheth, *Halo Models of Large Scale Structure*, *Phys. Rept.* **372** (2002) 1 [[astro-ph/0206508](#)].
- [3] M. Asgari, A.J. Mead and C. Heymans, *The halo model for cosmology: a pedagogical review*, *The Open Journal of Astrophysics* **6** (2023) .
- [4] R.H. Wechsler and J.L. Tinker, *The connection between galaxies and their dark matter halos*, *Annual Review of Astronomy and Astrophysics* **56** (2018) 435–487.
- [5] Z. Zhai and W.J. Percival, *Testing the framework of the halo occupation distribution with assembly bias modelling and empirical extensions*, *Mon. Not. Roy. Astron. Soc.* **535** (2024) 2469 [[2409.19399](#)].
- [6] B.D. Oppenheimer, G.M. Voit, Y.M. Bahé, N. Battaglia, J. Bregman, J.N. Burchett et al., *Introducing the descriptive parametric model: Gaseous profiles for galaxies, groups, and clusters*, 2025.
- [7] D. Ginzburg, V. Desjacques and K.C. Chan, *Shot noise and biased tracers: A new look at the halo model*, *Physical Review D* **96** (2017) .
- [8] A.Y. Chen and N. Afshordi, *Amending the halo model to satisfy cosmological conservation laws*, *Phys. Rev. D* **101** (2020) 103522 [[1912.04872](#)].
- [9] R.H. Liu, B. Hadzhiyska, S. Ferraro, S. Bose and C. Hernández-Aguayo, *Fast Baryonic Field Painting for Sunyaev-Zel’dovich Analyses: Transfer Function vs. Hybrid Effective Field Theory*, [2504.11794](#).
- [10] K.M. Smith, M.S. Madhavacheril, M. Münchmeyer, S. Ferraro, U. Giri and M.C. Johnson, *KSZ tomography and the bispectrum*, [1810.13423](#).

- [11] A. Vale and J.P. Ostriker, *Linking halo mass to galaxy luminosity*, *Monthly Notices of the Royal Astronomical Society* **353** (2004) 189 [<https://academic.oup.com/mnras/article-pdf/353/1/189/18655786/353-1-189.pdf>].
- [12] A.V. Kravtsov, A.A. Berlind, R.H. Wechsler, A.A. Klypin, S. Gottlöber, B. Allgood et al., *The Dark Side of the Halo Occupation Distribution*, *Astrophys. J.* **609** (2004) 35 [[astro-ph/0308519](#)].
- [13] C. Conroy, R.H. Wechsler and A.V. Kravtsov, *Modeling Luminosity-dependent Galaxy Clustering through Cosmic Time*, *Astrophys. J.* **647** (2006) 201 [[astro-ph/0512234](#)].
- [14] J. Jasche and B.D. Wandelt, *Bayesian physical reconstruction of initial conditions from large-scale structure surveys*, *Monthly Notices of the Royal Astronomical Society* **432** (2013) 894–913.
- [15] J. Jasche and B.D. Wandelt, *Methods for Bayesian Power Spectrum Inference with Galaxy Surveys*, *"Astrophys. J."* **779** (2013) 15 [[1306.1821](#)].
- [16] J. Jasche and G. Lavaux, *Matrix-free large-scale bayesian inference in cosmology*, *Monthly Notices of the Royal Astronomical Society* **447** (2014) 1204–1212.
- [17] G. Lavaux and J. Jasche, *Unmasking the masked Universe: the $2M^{++}$ catalogue through Bayesian eyes*, *"Mon. Not. Roy. Astron. Soc."* **455** (2016) 3169 [[1509.05040](#)].
- [18] R. von Marttens, L. Casarini, N.R. Napolitano, S. Wu, V. Amaro, R. Li et al., *Inferring galaxy dark halo properties from visible matter with machine learning*, *Monthly Notices of the Royal Astronomical Society* **516** (2022) 3924.
- [19] P. Villanueva-Domingo, F. Villaescusa-Navarro, D. Anglés-Alcázar, S. Genel, F. Marinacci, D.N. Spergel et al., *Inferring halo masses with graph neural networks*, *The Astrophysical Journal* **935** (2022) 30.
- [20] V.F. Calderon and A.A. Berlind, *Prediction of galaxy halo masses in SDSS DR7 via a machine learning approach*, *Mon. Not. Roy. Astron. Soc.* **490** (2019) 2367 [[1902.02680](#)].
- [21] M. de los Rios, M. Petač, B. Zaldivar, N.R. Bonaventura, F. Calore and F. Iocco, *Determining the dark matter distribution in simulated galaxies with deep learning*, *"Monthly Notices of the Royal Astronomical Society"* **525** (2023) 6015 [[2111.08725](#)].
- [22] C. Hahn, C. Bottrell and K.-G. Lee, *HaloFlow. i. neural inference of halo mass from galaxy photometry and morphology*, *The Astrophysical Journal* **968** (2024) 90.
- [23] S. Wu, N.R. Napolitano, C. Tortora, R. von Marttens, L. Casarini, R. Li et al., *Total and dark mass from observations of galaxy centers with machine learning*, *Astronomy & Astrophysics* **686** (2024) A80 [[2310.02816](#)].
- [24] V. Ono, C.F. Park, N. Mudur, Y. Ni, C. Cuesta-Lazaro and F. Villaescusa-Navarro, *Debiasing with diffusion: Probabilistic reconstruction of dark matter fields from galaxies with camels*, 2024.
- [25] C.F. Park, V. Ono, N. Mudur, Y. Ni and C. Cuesta-Lazaro, *Probabilistic reconstruction of dark matter fields from biased tracers using diffusion models*, 2023.
- [26] P.W. Battaglia, J.B. Hamrick, V. Bapst, A. Sanchez-Gonzalez, V. Zambaldi, M. Malinowski et al., *Relational inductive biases, deep learning, and graph networks*, 2018.
- [27] N. Garuda, J.F. Wu, D. Nelson and A. Pillepich, *Estimating dark matter halo masses in simulated galaxy clusters with graph neural networks*, 2024.
- [28] P. Villanueva-Domingo, F. Villaescusa-Navarro, D. Anglés-Alcázar, S. Genel, F. Marinacci, D.N. Spergel et al., *Inferring halo masses with graph neural networks*, *The Astrophysical Journal* **935** .
- [29] P. Villanueva-Domingo and F. Villaescusa-Navarro, *Learning cosmology and clustering with cosmic graphs*, *The Astrophysical Journal* **937** (2022) 115.

- [30] S. Ravanbakhsh, J. Oliva, S. Fromenteau, L.C. Price, S. Ho, J. Schneider et al., *Estimating cosmological parameters from the dark matter distribution*, 2017.
- [31] J. Schmelzle, A. Lucchi, T. Kacprzak, A. Amara, R. Sgier, A. Réfrégier et al., *Cosmological model discrimination with deep learning*, 2017.
- [32] A. Gupta, J.M.Z. Matilla, D. Hsu and Z. Haiman, *Non-gaussian information from weak lensing data via deep learning*, *Physical Review D* **97** (2018) .
- [33] D. Ribli, B.A. Pataki, J.M. Zorrilla Matilla, D. Hsu, Z. Haiman and I. Csabai, *Weak lensing cosmology with convolutional neural networks on noisy data*, *Monthly Notices of the Royal Astronomical Society* **490** (2019) 1843–1860.
- [34] J. Fluri, T. Kacprzak, A. Lucchi, A. Refregier, A. Amara, T. Hofmann et al., *Cosmological constraints with deep learning from kids-450 weak lensing maps*, *Physical Review D* **100** (2019) .
- [35] J.M.Z. Matilla, M. Sharma, D. Hsu and Z. Haiman, *Interpreting deep learning models for weak lensing*, *Physical Review D* **102** (2020) .
- [36] F. Villaescusa-Navarro, D. Anglés-Alcázar, S. Genel, D.N. Spergel, Y. Li, B. Wandelt et al., *Multifield cosmology with artificial intelligence*, 2021.
- [37] F. Villaescusa-Navarro, S. Genel, D. Angles-Alcazar, D.N. Spergel, Y. Li, B. Wandelt et al., *Robust marginalization of baryonic effects for cosmological inference at the field level*, 2021.
- [38] P. Villanueva-Domingo and F. Villaescusa-Navarro, *Removing astrophysics in 21 cm maps with neural networks*, *The Astrophysical Journal* **907** (2021) 44.
- [39] A. Lazanu, *Extracting cosmological parameters from n-body simulations using machine learning techniques*, *Journal of Cosmology and Astroparticle Physics* **2021** (2021) 039.
- [40] T. Lu, Z. Haiman and J.M. Zorrilla Matilla, *Simultaneously constraining cosmology and baryonic physics via deep learning from weak lensing*, *Monthly Notices of the Royal Astronomical Society* **511** (2022) 1518–1528.
- [41] Y. Kvasiuk, J. Krywonos, M.C. Johnson and M. Münchmeyer, *Reconstruction of Continuous Cosmological Fields from Discrete Tracers with Graph Neural Networks*, in *38th conference on Neural Information Processing Systems*, 11, 2024 [2411.02496].
- [42] F. Villaescusa-Navarro, D. Anglés-Alcázar, S. Genel, D.N. Spergel, R.S. Somerville, R. Dave et al., *The CAMELS Project: Cosmology and Astrophysics with Machine-learning Simulations*, *Astrophys. J.* **915** (2021) 71 [2010.00619].
- [43] F. Villaescusa-Navarro, S. Genel, D. Anglés-Alcázar, L.A. Perez, P. Villanueva-Domingo, D. Wadekar et al., *The CAMELS Project: Public Data Release*, *Astrophys. J. Suppl.* **265** (2023) 54 [2201.01300].
- [44] Y. Ni, S. Genel, D. Anglés-Alcázar, F. Villaescusa-Navarro, Y. Jo, S. Bird et al., *The CAMELS Project: Expanding the Galaxy Formation Model Space with New ASTRID and 28-parameter TNG and SIMBA Suites*, *Astrophys. J.* **959** (2023) 136 [2304.02096].
- [45] F. Villaescusa-Navarro, S. Genel, D. Angles-Alcazar, L. Thiele, R. Dave, D. Narayanan et al., *The CAMELS Multifield Dataset: Learning the Universe’s Fundamental Parameters with Artificial Intelligence*, *arXiv e-prints* (2021) arXiv:2109.10915 [2109.10915].
- [46] D. Sharma, B. Dai, F. Villaescusa-Navarro and U. Seljak, *A field-level emulator for modelling baryonic effects across hydrodynamic simulations*, *Mon. Not. Roy. Astron. Soc.* **538** (2025) 1415 [2401.15891].
- [47] N. Sehgal, P. Bode, S. Das, C. Hernandez-Monteagudo, K. Huffenberger, Y.-T. Lin et al., *Simulations of the microwave sky*, *The Astrophysical Journal* **709** (2010) 920–936.

- [48] G. Stein, M.A. Alvarez and J.R. Bond, *The mass-peak patch algorithm for fast generation of deep all-sky dark matter halo catalogues and itsn-body validation*, *Monthly Notices of the Royal Astronomical Society* **483** (2018) 2236–2250.
- [49] G. Stein, M.A. Alvarez, J.R. Bond, A.v. Engelen and N. Battaglia, *The websky extragalactic cmb simulations*, *Journal of Cosmology and Astroparticle Physics* **2020** (2020) 012–012.
- [50] S. Yasini, M. Alvarez, E. Schaan, K. Maamari, S.K. s. Mazinani, N. Mirzatanuny et al., *Astropaint: A python package for painting halo catalogs into celestial maps*, *Journal of Open Source Software* **5** (2020) 2608.
- [51] C. Modi, Y. Feng and U. Seljak, *Cosmological Reconstruction From Galaxy Light: Neural Network Based Light-Matter Connection*, *JCAP* **10** (2018) 028 [1805.02247].
- [52] B. Horowitz, C. Hahn, F. Lanusse, C. Modi and S. Ferraro, *Differentiable stochastic halo occupation distribution*, *Mon. Not. Roy. Astron. Soc.* **529** (2024) 2473 [2211.03852].
- [53] S. Wu, N.R. Napolitano, C. Tortora, R. von Marttens, L. Casarini, R. Li et al., *Total and dark mass from observations of galaxy centers with machine learning*, *Astronomy & Astrophysics* **686** (2024) A80.
- [54] M. Münchmeyer, M.S. Madhavacheril, S. Ferraro, M.C. Johnson and K.M. Smith, *Constraining local non-gaussianities with kinetic sunyaev-zel’dovich tomography*, *Physical Review D* **100** (2019) .
- [55] B. Hadzhiyska, L. Hernquist, D. Eisenstein, A.M. Delgado, S. Bose, R. Kannan et al., *The millenniumtnng project: refining the one-halo model of red and blue galaxies at different redshifts*, *Monthly Notices of the Royal Astronomical Society* **524** (2023) 2524–2538.
- [56] F. Villaescusa-Navarro, “Pylians: Python libraries for the analysis of numerical simulations.” Astrophysics Source Code Library, record ascl:1811.008, Nov., 2018.
- [57] H.L. Child, S. Habib, K. Heitmann, N. Frontiere, H. Finkel, A. Pope et al., *Halo profiles and the concentration–mass relation for a Λ CDM universe*, *The Astrophysical Journal* **859** (2018) 55.
- [58] Y. Wang, Y. Sun, Z. Liu, S.E. Sarma, M.M. Bronstein and J.M. Solomon, *Dynamic graph cnn for learning on point clouds*, *ACM Transactions on Graphics (tog)* **38** (2019) 1.
- [59] S. Ho, S. Dedeo and D. Spergel, *Finding the Missing Baryons Using CMB as a Backlight*, **0903.2845**.
- [60] P. Zhang, *The dark flow induced small-scale kinetic sunyaev–zel’dovich effect*, *Monthly Notices of the Royal Astronomical Society: Letters* **407** (2010) L36.
- [61] J. Shao, P. Zhang, W. Lin, Y. Jing and J. Pan, *Kinetic sunyaev-zel’dovich tomography with spectroscopic redshift surveys: Kinetic sz tomography*, *Monthly Notices of the Royal Astronomical Society* **413** (2011) 628–642.
- [62] D. Munshi, I.T. Iliev, K.L. Dixon and P. Coles, *Extracting the late-time kinetic Sunyaev–Zel’dovich effect*, *Mon. Not. Roy. Astron. Soc.* **463** (2016) 2425 [1511.03449].
- [63] A.-S. Deutsch, E. Dimastrogiovanni, M.C. Johnson, M. Münchmeyer and A. Terrana, *Reconstruction of the remote dipole and quadrupole fields from the kinetic Sunyaev Zel’dovich and polarized Sunyaev Zel’dovich effects*, *Phys. Rev. D* **98** (2018) 123501 [1707.08129].
- [64] J. Cayuso, R. Bloch, S.C. Hotinli, M.C. Johnson and F. McCarthy, *Velocity reconstruction with the cosmic microwave background and galaxy surveys*, *JCAP* **02** (2023) 051 [2111.11526].
- [65] F. McCarthy et al., *The Atacama Cosmology Telescope: Large-scale velocity reconstruction with the kinematic Sunyaev–Zel’dovich effect and DESI LRGs*, **2410.06229**.
- [66] R. Bloch and M.C. Johnson, *Kinetic Sunyaev Zel’dovich velocity reconstruction from Planck and unWISE*, **2405.00809**.

- [67] A. Laguë, M.S. Madhavacheril, K.M. Smith, S. Ferraro and E. Schaan, *Constraints on local primordial non-Gaussianity with 3d Velocity Reconstruction from the Kinetic Sunyaev-Zeldovich Effect*, [2411.08240](#).
- [68] J. Krywonos, S.C. Hotinli and M.C. Johnson, *Constraints on cosmology beyond Λ CDM with kinetic Sunyaev Zel'dovich velocity reconstruction*, [2408.05264](#).
- [69] A.C.M. Lai, Y. Kvasiuk and M. Münchmeyer, *KSZ Velocity Reconstruction with ACT and DESI-LS using a Tomographic QML Power Spectrum Estimator*, [2506.21684](#).
- [70] S.C. Hotinli, K.M. Smith and S. Ferraro, *Velocity Reconstruction from KSZ: Measuring f_{NL} with ACT and DESILS*, [2506.21657](#).
- [71] R.A. Sunyaev and Y.B. Zeldovich, *The velocity of clusters of galaxies relative to the microwave background. The possibility of its measurement*, *Monthly Notices of the Royal Astronomical Society* **190** (1980) 413.
- [72] Y. Kvasiuk and M. Münchmeyer, *Autodifferentiable likelihood pipeline for the cross-correlation of CMB and large-scale structure due to the kinetic Sunyaev-Zeldovich effect*, *Phys. Rev. D* **109** (2024) 083515 [[2305.08903](#)].
- [73] N. Battaglia, *The Tau of Galaxy Clusters*, *JCAP* **08** (2016) 058 [[1607.02442](#)].
- [74] M.S. Madhavacheril, N. Battaglia, K.M. Smith and J.L. Sievers, *Cosmology with the kinematic Sunyaev-Zeldovich effect: Breaking the optical depth degeneracy with fast radio bursts*, *Phys. Rev. D* **100** (2019) 103532 [[1901.02418](#)].
- [75] U. Giri and K.M. Smith, *Exploring KSZ velocity reconstruction with N-body simulations and the halo model*, *JCAP* **09** (2022) 028 [[2010.07193](#)].
- [76] J. Schaye et al., *The FLAMINGO project: cosmological hydrodynamical simulations for large-scale structure and galaxy cluster surveys*, *Mon. Not. Roy. Astron. Soc.* **526** (2023) 4978 [[2306.04024](#)].
- [77] R. Pakmor et al., *The MillenniumTNG Project: the hydrodynamical full physics simulation and a first look at its galaxy clusters*, *Mon. Not. Roy. Astron. Soc.* **524** (2023) 2539 [[2210.10060](#)].
- [78] C. Mondino, D. Pîrvu, J. Huang and M.C. Johnson, *Axion-induced patchy screening of the cosmic microwave background*, 2024.
- [79] F. McCarthy, D. Pîrvu, J.C. Hill, J. Huang, M.C. Johnson and K.K. Rogers, *Dark photon limits from patchy dark screening of the cosmic microwave background*, 2024.
- [80] D. Pîrvu, J. Huang and M.C. Johnson, *Patchy screening of the cmb from dark photons*, *Journal of Cosmology and Astroparticle Physics* **2024** (2024) 019.